

TiO₂ THIN FILM INTERLAYER FOR ORGANIC PHOTOVOLTAICS

by

Xin Wu

A Thesis Submitted to the Faculty of the

DEPARTMENT OF CHEMISTRY AND BIOCHEMISTRY

In Partial Fulfillment of the Requirements

For the Degree of

MASTER OF SCIENCE

WITH A MAJOR IN CHEMISTRY

In the Graduate College

THE UNIVERSITY OF ARIZONA

2015

STATEMENT BY AUTHOR

This thesis has been submitted in partial fulfillment of requirements for an advanced degree at the University of Arizona and is deposited in the University Library to be made available to borrowers under rules of the Library.

Brief quotations from this thesis are allowable without special permission, provided that an accurate acknowledgement of the source is made. Requests for permission for extended quotation from or reproduction of this manuscript in whole or in part may be granted by the head of the major department or the Dean of the Graduate College when in his or her judgment the proposed use of the material is in the interests of scholarship. In all other instances, however, permission must be obtained from the author.

SIGNED: Xin Wu

APPROVAL BY THESIS DIRECTOR

This thesis has been approved on the date shown below:

_____	_____ 6/17/2015 _____
Neal R. Armstrong	Date
Regents Professor of	
Chemistry/Biochemistry/Optical Sciences	

ACKNOWLEDGEMENT

I would like to express my sincere thanks to my advisor Prof. Neal R. Armstrong for his valuable support and guidance throughout the research process. I am very grateful to my committee members, Prof. Scott S. Saavedra, Prof. Oliver A. Monti, and Prof. Jeanne E. Pemberton, for their time and efforts in advising me. I would like to thank deeply all the individuals who have helped me to become a better researcher and contributed to this research and thesis.

Table of Contents

List of Figures	6
List of Tables.....	10
Abstract	11
Chapter 1: Introduction	12
1.1 Organic Solar Cells	12
1.1.1 Solar Cells in Global Energy Demand	12
1.1.2 Solar Cells	13
1.1.3 Organic Solar Cells.....	15
1.1.4 Characterization of Organic Photovoltaic Cells (OPV).....	17
1.2 TiO ₂ Charge Selective Interlayer.....	20
1.2.1 Charge Selective Interlayers.....	20
1.2.2 TiO ₂ as Electron Selective Interlayer	22
1.2.3 TiO ₂ Film Preparation	23
1.2.4 Chemical Vapor Deposition (CVD) and Atomic Layer Deposition (ALD).....	24
1.3 Research Overview.....	28
Chapter 2: Experimental.....	30
2.1 Chemical Vapor Deposition of TiO ₂ Films on ITO.....	30
2.2 Atomic Layer Deposition of TiO ₂ Films on ITO	31
2.3 CAFM Characterization of Roughness, Morphology and Conductivity	32

2.4 XPS Characterization of TiO ₂ Films on ITO.....	33
2.5 Cyclic Voltammetry Characterization of ALD TiO ₂ Films on ITO	33
2.6 Device Fabrication	34
2.7 Device Characterization	34
Chapter 3: Results and Discussion	35
3.1 The Morphology and Conductivity of TiO ₂ Films prepared by CVD and ALD.....	35
3.2 ITO/TiO ₂ Surface Composition (XPS).....	45
3.3 Charge Blocking Behavior (CV).....	51
3.4 Device Characterization	60
Chapter 4: Conclusions and Future Directions.....	65
4.1 Conclusions.....	65
4.2 Future Directions.....	66
References	67

List of Figures

Figure 1. Global capacity growth in solar PV market (from Renewables 2014 Global Status Report, used with permission from REN21).....	12
Figure 2. The best research-cell efficiencies maintained by National Renewable Energy Laboratory (NREL). The chart is downloaded on April 1, 2015. (This figure is in the public domain in the United States.)	15
Figure 3. Cross-section of three different architectures of organic solar cells as they develop. (a) Single layer homojunction; (b) bi-layer heterojunction; (c) bulk heterojunction. ...	16
Figure 4. Photocurrent generation process. (a) Light absorption. (b) Exciton diffusion. (c) Exciton dissociation. (d) Charge migration and charge collection.....	18
Figure 5. The equivalent circuit model of a solar cell. It contains a photocurrent source (J_{ph}), a diode, a series resistor (R_s) and a shunt resistor (R_p).....	19
Figure 6. Characteristic current density - voltage (J - V) curves of an organic solar cell under dark (blue line) and illuminated (red line) conditions.	20
Figure 7. Conventional (left) and inverted (right) device structures. P3HT:PCBM is the light absorbing active layer. TiO_2 is the electron selective interlayer material. PEDOT: PSS is the hole selective interlayer material. ITO and metals are the electrodes. The polarity of the device is determined by the interlayer material.....	22
Figure 8. (a) Energy level diagram of common charge selective interlayers utilized in OPVs. ³³ P3HT and PCBM are added as references. (b) Illustration of the hole blocking and electron harvesting property of the TiO_2 electron collection layer.	23
Figure 9. Schematic illustration of the CVD process.	25

Figure 10. Schematic illustration of the ALD process.	27
Figure 11. Schematic view of the CVD system.....	31
Figure 12. Schematic view the ALD system.	32
Figure 13. Contact mode CAFM images and associated histograms of bare ITO and ITO/TiO ₂ samples. (a) Height image of bare ITO. (b) Current image of bare ITO at -0.100 V bias. (c) Height image of ITO/(CVD 24 nm)TiO ₂ . (d) Current image of ITO/(CVD 24 nm)TiO ₂ at -4.000 V bias. (a.his) Associated histogram of image a with bin size of 0.2 nm. (b.his) Associated histogram of image b with a bin size of 50 pA. (c.his) Associated histogram of image c with bin size of 0.2 nm. (d.his) Associated histogram of image d with a bin size of 50 pA.....	37
Figure 14. (a) Schematic diagram of CAFM measurements and proposed (b) pre-contact energy levels of materials used in measurement.	38
Figure 15. Contact mode CAFM images and associated histograms of bare ITO and ITO/TiO ₂ samples. (a) Height image of bare ITO. (b) Current image of bare ITO at -1.000 V bias. (c) Height image of ITO/(ALD 1 nm)TiO ₂ . (d) Current image of ITO/(ALD 1 nm)TiO ₂ at -2.000 V bias. (e) Height image of ITO/(ALD 3 nm)TiO ₂ . (f) Current image of ITO/(ALD 3 nm)TiO ₂ at -2.000 V bias. (g) Height image of ITO/(ALD 10 nm)TiO ₂ . (h) Current image of ITO/(ALD 10 nm)TiO ₂ at -1.500 V bias. (a.his) Associated histogram of image a with bin size of 0.2 nm. (b.his) Associated histogram of image b with a bin size of 50 pA. (c.his) Associated histogram of image c with bin size of 0.2 nm. (d.his) Associated histogram of image d with a bin size of 50 pA. (e.his) Associated histogram of image e with bin size of 0.2 nm. (f.his) Associated histogram of image f with a bin size of 50 pA. (g.his) Associated histogram of image g	

with bin size of 0.2 nm. (h.his) Associated histogram of image h with a bin size of 50 pA.	43
Figure 16. GIXRD patterns of a 10 nm (blue line) and 5 nm (green line) TiO ₂ films deposited on Si with 0.18° incidence angle. The red lines give the XRD pattern of reference anatase TiO ₂ (PDF 01-070-7348). Image is provided by the Graham group at Georgia Institute of Technology.....	45
Figure 17. Ti 2p XPS spectra for ITO/TiO ₂ samples. (a) ITO/(ALD 0.5 nm)TiO ₂ , (b) ITO/(ALD 1 nm)TiO ₂ , (c) ITO/(ALD 3 nm)TiO ₂ , (d) ITO/(CVD 24 nm)TiO ₂	46
Figure 18. In 3d XPS spectra for ITO/TiO ₂ samples. (a) ITO/(ALD 0.5 nm)TiO ₂ , (b) ITO/(ALD 1 nm)TiO ₂ , (c) ITO/(ALD 3 nm)TiO ₂ . Measurements were taken at 0° (red dashed lines) and 60° (black dashed lines) take-off angles for each sample.	48
Figure 19. O 1s XPS spectra for ITO/TiO ₂ samples. (1) ITO/(ALD 0.5 nm)TiO ₂ , (2) ITO/(ALD 1 nm)TiO ₂ , (3) ITO/(ALD 3 nm)TiO ₂ . O 1s component ‘a’ at 530.0 eV is attributed to TiO ₂ and ITO O ²⁻ . O 1s component ‘b’ at 531.3 eV is attributed to the hydroxyl group. O 1s component ‘c’ at 532.3 eV is attributed to C-O.	50
Figure 20. (a) Electrochemical probe molecules. (b) Illustration of TiO ₂ blocking electrochemical activity of probe molecules.	53
Figure 21. Cyclic voltammograms of probe molecules Decamethylferrocene, 1,1-Dimethylferrocene, and TPD(N,N’ -Bis(3-methylphenyl)-N,N’ -diphenylbenzidine) with a) bare ITO electrode, b) ITO/(ALD 0.5 nm)TiO ₂ , c) ITO/(ALD 1 nm)TiO ₂ , d) ITO/(ALD 3 nm)TiO ₂ , e) ITO/(ALD 10 nm)TiO ₂ . The potential was scanned at 0.05 V/s vs Ag/Ag ⁺ reference electrode.	56

Figure 22. (a) Proposed general band energy diagram of Ag/p-type Si/TiO_x/Al test device structures. (b) Current density-voltage (*J-V*) characteristics of Al/p-type Si/Ag or Al/n-type Si/Ag devices with or without 3 nm TiO₂ hole-blocking layer between the Al contact and Si. 59

Figure 23. Current density-voltage characteristics of ITO/TiO₂/P₃HT:PC₆₁BM/PEDOT:PSS/Ag photovoltaic devices with different TiO₂ interlayers. (a) Log *J-V* curves under dark conditions. (b) Linear *J-V* curves under illumination..... 62

Figure 24. Device configuration (bottom) of ITO/TiO₂/P₃HT: PC₆₁BM/PEDOT: PSS/Ag photovoltaic devices and its proposed band diagram (top) from literature values. 64

Figure 25. Ideality factor – Voltage characteristics calculated for the photovoltaic devices with ALD TiO₂ films of different thicknesses..... 64

List of Tables

Table 1. Summary of Contact mode CAFM results. Sigma is obtained assuming the current distribution is Gaussian.	44
Table 2. Summary of analysis of binding energy results from XPS for Ti 2p peaks.	47
Table 3. % composition of O 1s components from XPS thickness varied ITO/TiO ₂ samples.	51
Table 4. Summary of experimental determined and tunneling model predicted heterogeneous electron transfer rate constant (<i>ks</i>) of dimethylferrocene base on the values of the peak separations.	58
Table 5. Summary of ITO/TiO ₂ /P ₃ HT:PC ₆₁ BM/PEDOT: PSS/Ag photovoltaic device characteristics with different TiO ₂ interlayers. 0.5, 1, 3 and 10 nm thick TiO ₂ interlayers were ALD films and 24 nm thick TiO ₂ interlayer was CVD film. Shunt resistance (<i>R_p</i>) is estimated from the inverted slope of light <i>J-V</i> curves at -1.0 V. Series resistance (<i>R_s</i>) is estimated from the inverted slope of light <i>J-V</i> curves at +1.0 V. The local ideality factor (<i>n</i>) of the device is determined in the low voltage region.	61

Abstract

TiO₂ films as electron collecting interlayers are important in determining the efficiency of organic photovoltaics (OPVs). Various methods of film deposition have been explored, and they revealed the tradeoff between pinhole free coverage (large shunt resistance) and small film thickness (small series resistance). It is hypothesized that atomic layer deposition (ALD) with its self-limiting nature and sub-nanometer level control would be able to circumvent this problem and provide TiO₂ films of pinhole free coverage and small thickness.

TiO₂ films made by chemical vapor deposition (CVD) and ALD were investigated and compared. Conductive atomic force microscopy (CAFM) was used to characterize film morphology and conductivity. X-ray photoelectron spectroscopy (XPS) was utilized to analyze film composition and chemical state. Cyclic voltammetry (CV) was able to reveal the hole blocking capability of films. Finally, organic photovoltaic devices were made with different TiO₂ films to reveal the relationship between device property and film characteristic. It is found that both CVD and ALD created TiO₂ films with Ti⁴⁺ species containing oxygen from hydroxyl groups. They both showed conformal coverage of the electrode via CAFM and CV measurements, and clearly ALD method achieved this with a thinner film and smaller series resistance. This work provided the evidence of effective and surprising capabilities of electron harvesting and hole blocking of ultrathin ALD TiO₂ films for OPVs.

Chapter 1: Introduction

1.1 Organic Solar Cells

1.1.1 Solar Cells in Global Energy Demand

In Renewables 2014 Global Status Report (GSR), renewable energy provided about 19% of global energy consumption in 2012 and is considered crucial by more and more countries for current and future energy needs. In 2013, solar power takes up 53% of the global new investment in renewable power and fuels, making it the leading sector again. Over the past five years, solar photovoltaics (PVs) has expanded in capacity with a rapid average rate of 55% annually. Also, according to 2014 GSR, PV market had a record year in 2013 by adding more than 39 GW in solar PV capacity for a total exceeding 139 GW (Figure 1). Solar cells' significant role in the provision of renewable energy services stimulates continued scientific research for more efficient and lower-cost PV cells (Figure 1).

Solar PV Total Global Capacity, 2004–2013

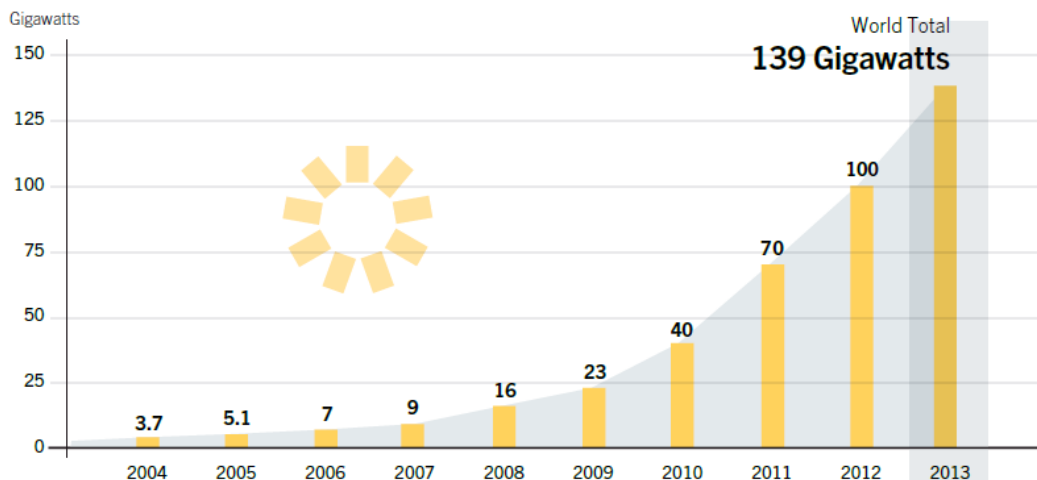


Figure 1. Global capacity growth in solar PV market (from Renewables 2014 Global Status Report, used with permission from REN21).

1.1.2 Solar Cells

PV cells based on crystalline silicon as the absorber layer are considered as first generation solar cells and are taking up a major portion of the current PV market. Figure 2 shows the best research-cell efficiencies from 1975 to current.

The highest efficiency achieved by crystalline silicon solar cells (with concentrator) has been ca. 27.6%. In a crystalline silicon solar cell, incident photons with energies higher than the band gap energy will generate electron-hole pairs. A carrier selective p-n junction will direct electrons and holes to their respective sides to be collected. A photon with less energy than the band gap energy will not be able to generate an electron-hole pair. Photons with energies greater than the band gap energy will excite electrons to states above the band gap and the excited electrons will dissipate its extra energies through relaxation. Materials with smaller band gap will capture more photons with less energy per photon, while materials with larger band gap will capture less photons with more energy per photon. An analysis of the standard AM 1.5 solar spectrum¹ shows the best balance is reached at 1.34 eV giving a 33.7% efficiency, the Shockley–Queisser limit.² Silicon has a band gap of 1.1 eV, resulting in a 29% efficiency limit for single junction cells.

Multi-junction PV cells and the thin-film category, including Cadmium Telluride (CdTe), copper indium gallium selenide (CIGS) and amorphous silicon (a-Si) solar cells, are called second generation solar cells and are gaining more and more market share.

Multi-junction PV cells made with multiple materials have multiple band gaps and are able to capture energies which would otherwise be lost by relaxation in single-junction solar cells. The highest-efficiency research cell shown was achieved in multi-junction cells used in concentrated photovoltaic (CPV) systems at 46.0% efficiency. Under concentrated sunlight, the limiting efficiency of cells with infinite number of junctions is 86%.³ Multi-junction PV cells' high

efficiency comes with increased complexity and a higher price, and makes them the preferable choice in the aerospace or in terrestrial applications in concentrated photovoltaics.

Crystalline silicon (c-Si) solar cells use silicon wafers that are typically hundreds of micrometers thick, because crystalline silicon is an indirect-gap material where light can penetrate much farther before being absorbed than in a direct band gap material. Thin-film solar cells use direct-gap materials like CdTe and CIGS, which can absorb enough light with much thinner thickness and are typically made less than one micrometer thick. Thin-film solar cells are developed in an effort to bring down manufacturing cost and material usage. The top efficiency reported for thin-film technologies is 23.3% with CIGS (concentrator). Thin-film solar cells are less efficient but they require less material and could be made flexible and lighter for various applications.

Third generation of solar cells are made up of a number of emerging photovoltaics in research and development, which includes dye-sensitized, quantum dots, perovskite and organic/polymer solar cells.

The biggest problem with conventional solar cells are their expensive materials and manufacturing process. Efforts have been directed to develop solar cells that use materials other than silicon and could be solution processed. Dye-sensitized, quantum dots, perovskite and organic/polymer solar cells have respectively reported best research-cell efficiencies of 11.9%, 9.9%, 20.1%(not stabilized), and 11.1% (Figure 2). Commercial applications of these cells would be held up until their chemical stability problems are better addressed and higher efficiencies are still under pursuit.

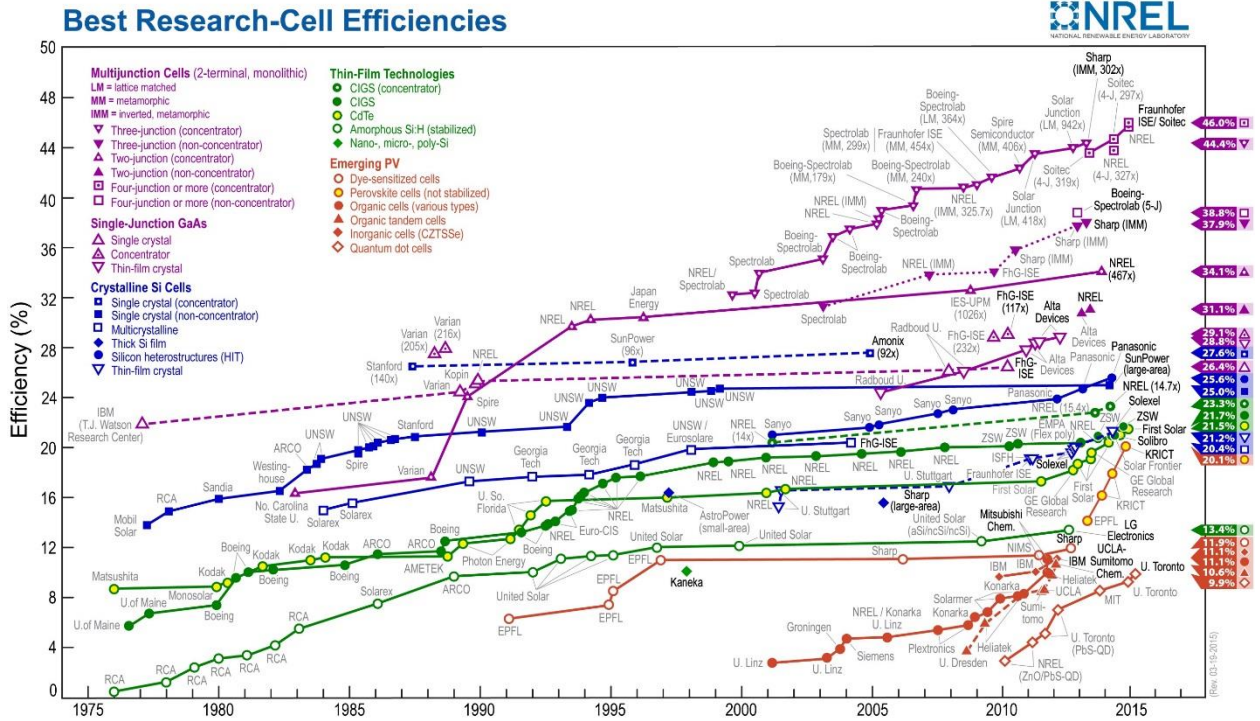


Figure 2. The best research-cell efficiencies maintained by National Renewable Energy Laboratory (NREL).

The chart is downloaded on April 1, 2015. (This figure is in the public domain in the United States.)

1.1.3 Organic Solar Cells

Organic solar cells have the potential to realize the production of low-cost, large-area, flexible and lightweight photovoltaic devices.⁴⁻⁵ In an organic solar cell, organic electronic materials like organic small molecules or polymers are used as the absorbing photovoltaic materials. Figure 3 shows three different structures of organic solar cells as they develop. Rather than the free electron-hole pairs as generated in inorganic solar cells, excitons (coulombically bound electron-hole pairs) are generated when light is absorbed by organic materials. The exciton binding energy is on the order of 0.2 – 0.5 eV, which is much higher than the thermal energy $k_B T$ (0.0257 eV).⁶ The exciton diffusion length are typically 1-10 nm, thus in early homojunction organic solar cells most of the excitons are lost through recombination before they can dissociate upon reaching the electrode.⁴

Tang's work introduced the bi-layer structured organic active layer providing an organic donor/acceptor interface which would dissociate excitons much more effectively than an organic/metal interface. This brought the device efficiencies from the order of 0.1% to 1%. The idea of exciton dissociating at the heterojunction is that it is thermodynamically favorable for the electron to transfer from the donor to acceptor when the donor material has a higher lowest unoccupied molecular orbital (LUMO) level than the acceptor material, and the energy difference between their LUMO levels is larger than the exciton binding energy. The exciton needs to diffuse to a donor/acceptor materials interface within its lifetime and dissociate into free charge carriers in order for energy to be harvested. In a planar heterojunction organic solar cell, exciton diffusion length constrains the thickness of the photoactive layer, because only excitons formed within their diffusion length to the interface would not decay before separation. The bulk heterojunction solar cell came with further enhanced efficiencies by overcoming this thickness limit and increasing the interface area (orders of magnitude).⁷ The blended donor and acceptor material in bulk heterojunction solar cell creates a percolating network with the size of its donor domain close to the exciton diffusion length. Free charge carriers generated at the interface can be transported through the percolating network of donor and acceptor domains to their respective electrodes. Holes will be collected at the anode and electrons will be collected at the cathode.

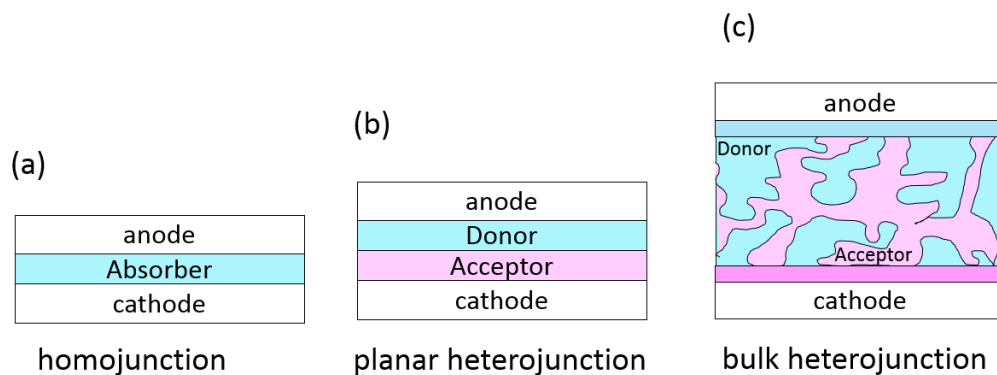


Figure 3. Cross-section of three different architectures of organic solar cells as they develop. (a) Single layer homojunction; (b) bi-layer heterojunction; (c) bulk heterojunction.

1.1.4 Characterization of Organic Photovoltaic Cells (OPV)

The photocurrent generating process is schematically summarized in Figure 4.⁸ Each step in the process has its corresponding efficiency. The internal quantum efficiency is the product of the step efficiencies:

$$\eta_{IQE} = \eta_A \eta_{ED} \eta_{CT} \eta_{CC} \quad (\text{Equation 1})$$

where η_{IQE} is internal quantum efficiency, defined as the fraction of collected carriers per absorbed photon; η_A is light absorption efficiency, which is the ratio of the number of excitons generated to the number of incident photons; η_{ED} is exciton diffusion efficiency, determined by the ratio of excitons arrived at the dissociation site to the total number of excitons generated; η_{CT} is charge transfer efficiency, which is the efficiency of onsite excitons dissociating into free charge carriers; η_{CC} is charge collection efficiency, defined as the ratio of the number of charge carriers generated to the number of charge carriers collected. The external quantum efficiency has the optical losses taken into account:

$$\eta_{EQE} = \eta_{IQE}(1 - R) \quad (\text{Equation 2})$$

where η_{EQE} is external quantum efficiency; R is the reflectivity of the substrate-air interface. The increase in overall cell efficiency is based on the improvement of efficiency at each stage. Active layers with large absorption coefficients and a better match with the solar spectrum are used to increase absorption efficiency.⁹ Strong absorption coefficient of organic active layers enabled efficient light absorption with films of thicknesses of only 100-200 nm. In a bi-layer structure, there is a tradeoff between light absorption and exciton diffusion efficiencies. The bulk heterojunction structure was introduced to overcome this problem. With the discovery of conjugated polymer-fullerene composites, the charge transfer efficiency in a bulk heterojunction solar cell is approaching unity.¹⁰ Charge collection efficiency is a function of charge carrier mobility and charge transfer rate across organic/electrode interface.

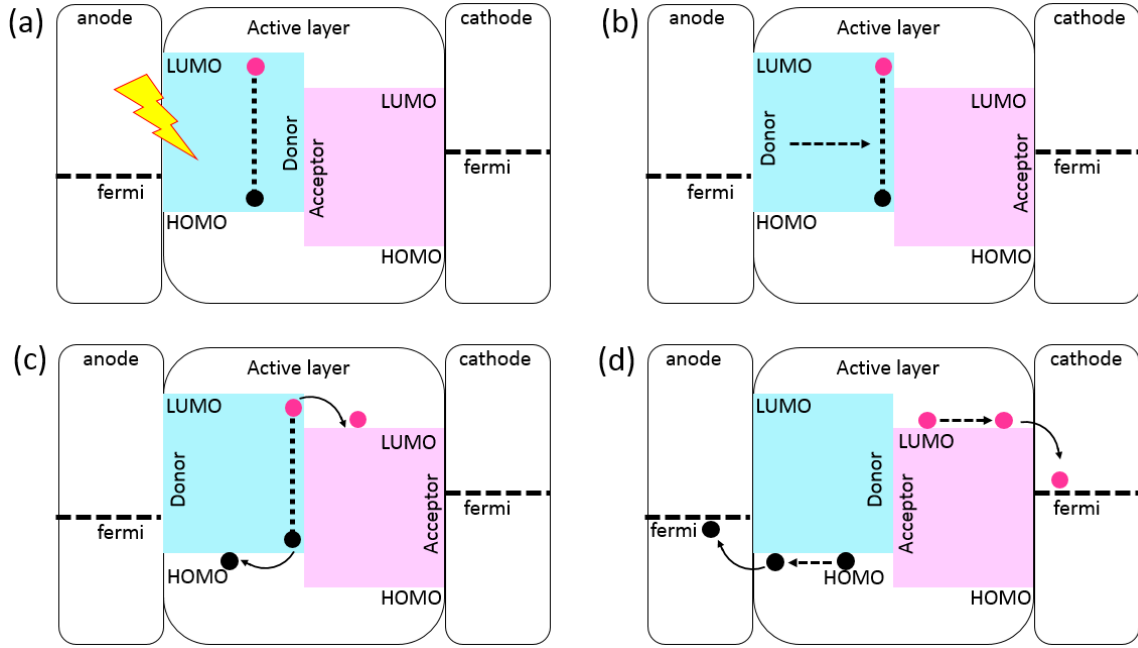


Figure 4. Photocurrent generation process. (a) Light absorption. (b) Exciton diffusion. (c) Exciton dissociation. (d) Charge migration and charge collection.

Figure 5 shows the widely used equivalent circuit model for a solar cell. It contains a photocurrent source, a diode, a series resistor and a shunt resistor. J_{ph} represents the photocurrent under illumination. J_{ph} is zero under dark conditions and is proportional to light intensity. The diode accounts for the rectifying behavior of the donor/acceptor heterojunction. R_s is series resistance. It accounts for bulk, interface and contact resistances for the cell. Series resistance should be minimized to reduce electrical power losses. R_p is shunt resistance. Shunt resistance accounts for the leakage current, which causes power losses. Shunt resistance should be maximized by preventing pinholes and reducing recombination in the device. This model describes the photovoltaic behavior as:¹¹

$$J = J_0 \left[\exp \left(\frac{e(V - JR_s)}{nk_B T} \right) - 1 \right] + \frac{V - JR_s}{R_p} - J_{ph} \quad (\text{Equation 3})$$

where J_0 is the reverse saturation current (leakage current), e is the elementary charge, n is the ideality factor, k_B is the Boltzmann constant, T is absolute temperature.

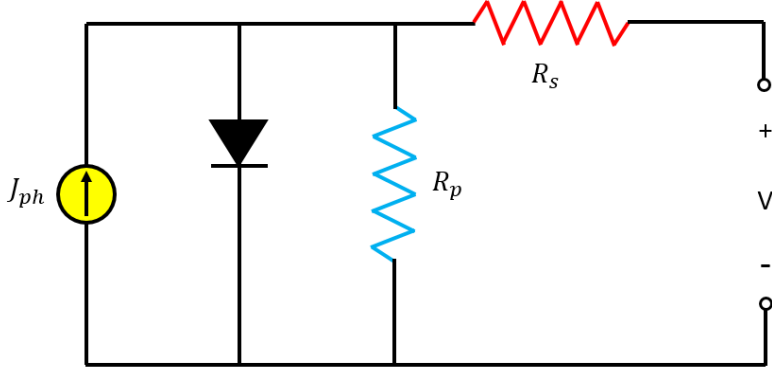


Figure 5. The equivalent circuit model of a solar cell. It contains a photocurrent source (J_{ph}), a diode, a series resistor (R_s) and a shunt resistor (R_p).

Figure 6 shows the characteristic current density - voltage (J - V) curves of an idealized organic solar cell. The maximum power point is found where the product of current and voltage is at its largest. V_{oc} is the open circuit voltage, J_{sc} is the short circuit current. Fill factor (FF) is defined as $(V_{max} \times J_{max}) / (V_{oc} \times J_{sc})$. The power conversion efficiency (η) is the percentage ratio of the device maximum power (P_{max}) to the total incident power (P_{in}):

$$\eta = \frac{P_{max}}{P_{in}} = \frac{V_{max} \times J_{max}}{P_{in}} = \frac{V_{oc} \times J_{sc} \times FF}{P_{in}} \quad (\text{Equation 4})$$

This above equation states that the power conversion efficiency is linearly dependent on open circuit voltage, short-circuit current and the fill factor. V_{oc} is dependent to a first

approximation on the difference between the highest occupied molecular orbital (HOMO) level of the donor and the lowest unoccupied molecular orbital (LUMO) level of the acceptor.¹² J_{sc} depends on the energy difference between the LUMOs of the donor and the acceptor as well as the charge-carrier mobility. Organic semiconductors generally exhibit mobilities in the 10^{-5} to 10^0 cm^2/Vs range. This limits the active layer thickness in OPVs, since charge carriers need to reach the electrodes before recombination.¹³ Several interacting factors affect the FF of a solar cell in complex ways, and generally FF accounts for the charge recombination in a cell.¹²

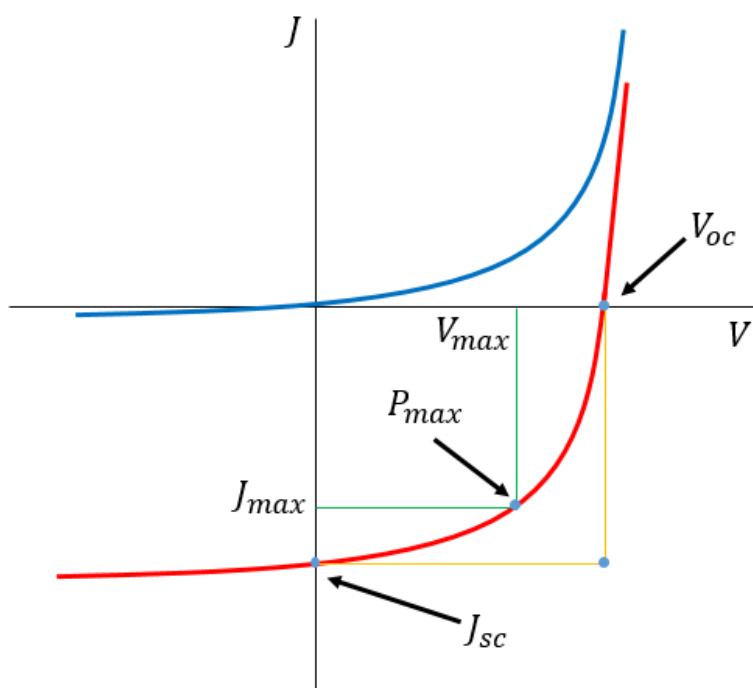


Figure 6. Characteristic current density - voltage (J - V) curves of an organic solar cell under dark (blue line) and illuminated (red line) conditions.

1.2 TiO_2 Charge Selective Interlayer

1.2.1 Charge Selective Interlayers

In bulk heterojunction solar cell, the polarity of the solar cell is controlled by the electrode.¹⁴⁻¹⁵ The conventional bulk heterojunction structure has its polymer donor and fullerene acceptor blend

sandwiched between a high work function transparent oxide anode, most commonly indium tin oxide (ITO), and a low work function metal cathode (e.g. aluminum, calcium).¹⁶ Instability of the device was demonstrated by the fact that indium atoms in the transparent electrode ITO have been observed to diffuse through the layers in the device and end up in the counter electrode.¹⁷ And there is also device decay associated with aluminum/organic interface reaction and oxygen or water diffusion through the reactive metal electrode.¹⁸⁻¹⁹ In addition to in-diffusion, the organic/electrode interface dipole formation, charge transfer, chemical reaction and energy level alignment all have profound impact on device performance.²⁰ The importance of organic/electrode interface has led to the efforts in modification of electrode contacts with interlayers (e.g., small molecules, conductive polymers and metal oxides). Discoveries were made that interlayers inserted between the electrode and organic active layer would not only enhance the cell stability, but also increase the cell efficiency by providing better contact properties at the organic/electrode interface.²⁰⁻²¹ Interlayers with high work function like PEDOT: PSS²², V₂O₅²³, NiO_x²⁴, WO₃²⁵, and MoO₃²⁶ were introduced between the active organic layer and oxide electrode to facilitate the hole collection at the cathode.²² And devices with anode interlayer materials like LiF²⁷, Cs₂O₃²⁸ also exhibited enhanced cell efficiency and stability. Still, the inherent instability of reactive low work function metal electrode lead to the design of inverted device structure (Figure 7), where the electron collection happens on the transparent ITO side with an electron selective interlayer, and stable metals like Au and Ag were used as the hole collection anode.²⁹ This inverted structure also avoids the direct contact between the widely used hole extraction layer PEDOT: PSS and ITO, which is beneficial because the ITO/PEDOT: PSS was not stable³⁰. In the inverted structure, TiO₂³¹ and ZnO³² are the most investigated electron collection metal oxide interlayer materials.

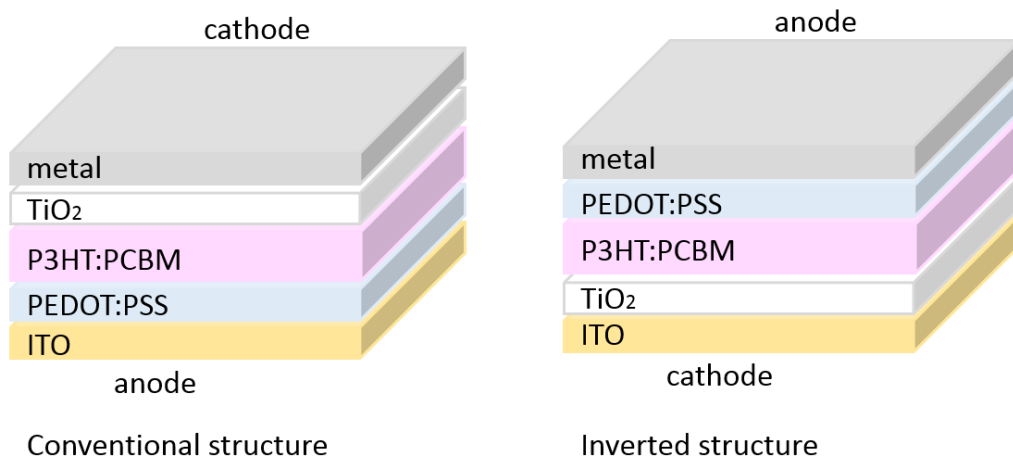


Figure 7. Conventional (left) and inverted (right) device structures. P3HT:PCBM is the light absorbing active layer. TiO₂ is the electron selective interlayer material. PEDOT: PSS is the hole selective interlayer material. ITO and metals are the electrodes. The polarity of the device is determined by the interlayer material.

1.2.2 TiO₂ as Electron Selective Interlayer

The charge selectivity of metal oxide interlayer materials originates from their wide band gap and energy level alignment with the electron transporting or hole transporting in organic active layers. Figure 8 shows the energy levels of common charge selective interlayers utilized in OPVs.³³ The energy barrier for electron collection depends on the energy level difference between the LUMO of organic acceptor and the conduction band (CB) of the metal oxide. The energy level difference between the HOMO of organic donor and the valence (VB) of the metal oxide controls the energy barrier for hole collection. Aligned energy levels enable easier establishment of electronic equilibrium and smaller charge collection barrier.^{24, 34} TiO₂ along with ZnO are popular candidates for electron collection interlayers. The conduction band of TiO₂ is positioned close the LUMO level of the common organic acceptor PCBM. The HOMO of the common organic donor P3HT lies in the wide band gap of TiO₂, which adds the hole blocking behavior to the interlayer (Figure 8). Both ZnO and TiO₂ exhibited higher electron mobility than hole mobility, which makes them ideal electron transport layer. ZnO was favored for its higher electron mobility than TiO₂³⁴⁻³⁵, and TiO₂ has its advantage of making more stabilized device.³⁶⁻³⁸ It was reported that a sealed

device with ZnO interlayer retained 80.7% of its initial efficiency under 40 h of illumination³⁹, and sealed device with TiO₂ interlayer retained 96.3% of its initial efficiency under 120 h of illumination³⁸. Methods like annealing⁴⁰ and doping⁴¹ were used to enhance the electron mobility of TiO₂. It was not never explored, however, how far we can go to reduce TiO₂ film thickness to compensate for its smaller electron mobility.

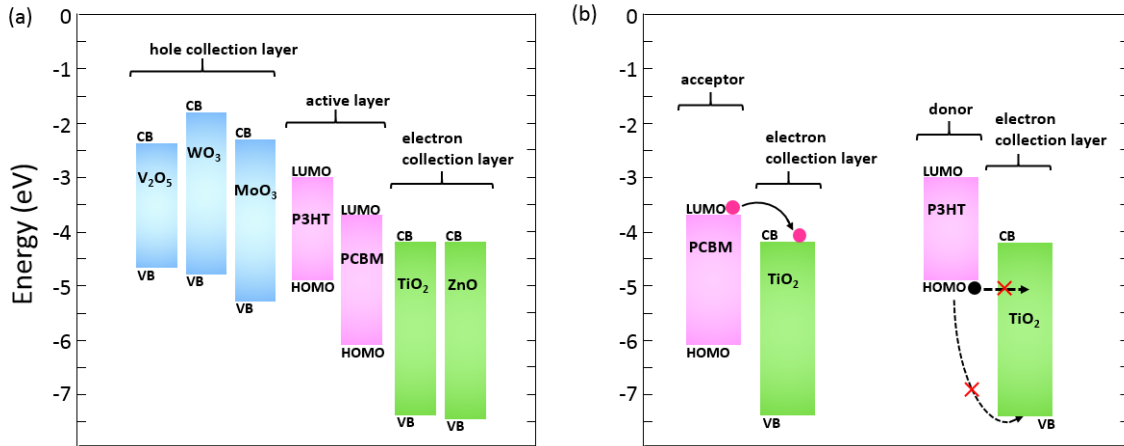


Figure 8. (a) Energy level diagram of common charge selective interlayers utilized in OPVs.³³ P3HT and PCBM are added as references. (b) Illustration of the hole blocking and electron harvesting property of the TiO₂ electron collection layer.

1.2.3 TiO₂ Film Preparation

There are numerous methods established for the preparation of TiO₂ films⁴², which is largely due to its wide application in sensors, photo catalysis and dye sensitized solar cells.⁴³⁻⁴⁶ Methods like sputtering⁴⁷, chemical vapor deposition⁴⁸ and sol-gel³⁶ have seen their application in making TiO₂ films for bulk heterojunction solar cells. The benefit of sol-gel methods, which includes low-temperature solution processability⁴⁹ and capability in nanoparticle synthesis⁴⁴, has drawn the interest of many researchers and made it a popular method to prepare TiO₂ film for OPVs. The sol-gel prepared TiO₂ film features a porous film with many protrusions.⁴⁹⁻⁵⁰ The porosity of the film

can lead to incomplete electrode coverage, which would result in undesired charge recombination at pinholes. One way to reduce this recombination is to increase the thickness of the TiO₂ layer, however, thicker films often result in larger series resistance.⁵¹ Therefore, there is a tradeoff between small film thickness and pinhole free coverage, which is equivalent to a tradeoff between small series resistance and high electron selectivity (or large shunt resistance).³⁸ To break this constraint, efforts have been made to increase the electron mobility or improve film coverage, but that requires high temperature treatment (ca. 450°C),^{41, 52-53} which takes away the very important merit of sol-gel processing: low temperature. Hence the conformal coverage of electrode with small film thickness is of interest. Chemical vapor deposition (CVD) has been demonstrated to provide thin TiO₂ films (24 nm) with pinhole free electrode coverage.⁴⁸ Atomic layer deposition (ALD) is unique amongst thin film preparation methods because of the self-terminated layer-by-layer reaction process, which enables ALD to deliver films with even better conformity than CVD.⁵⁴ Thus atomic layer deposition becomes an attractive candidate for OPV interlayers for its excellent conformity and thickness control.⁵⁴⁻⁵⁶ It is reported that 20 nm thick ALD ZnO films delivered OPVs with better performance than sol-gel ZnO of the same thickness.⁵⁷ Due to the stability issues discussed in the previous section,³⁸⁻³⁹ it is of more importance and interest to explore the property of ALD TiO₂ film for OPV application.

1.2.4 Chemical Vapor Deposition (CVD) and Atomic Layer Deposition (ALD)

For a long time in modern deposition of metal oxide films, both CVD and ALD are of prime importance in microelectronic manufacturing process.⁵⁸ They can be used to grow films with controlled thickness, composition and doping, and they yield conformal coverage on non-planar geometries with high film uniformity.⁵⁸⁻⁵⁹ This makes them excellent candidates as deposition methods for pinhole-free metal oxide interlayers in organic photovoltaic devices.⁴⁸

CVD is defined as a process whereby a thin solid film is deposited onto a substrate through chemical reactions of the gaseous species.⁶⁰ The deposition of TiO₂ film by CVD using titanium-tetraisopropoxide (TTIP) as a precursor (reactant gas) is illustrated in Figure 9.⁶¹⁻⁶² Gaseous TTIP are generated by bubbling method in the vapor precursor supply system and transported into the reaction chamber. TTIP then diffuse through the boundary layer and adsorb on the substrate. At the interface of gas and heated substrate, decomposition occurs to produce deposits and by-products. Deposits will diffuse along the heated substrate surface and by-products will be removed from the boundary layer via diffusion or convection. The unreacted gaseous reactants and by-products are carried away from the reaction chamber.

The properties of deposited film, like chemical composition, crystalline nature, uniformity and so on, strongly depends on the processing parameters, such as the nature of precursor, flow rate and temperature.⁶⁰ With CVD method, layer thickness can be controlled from the micrometer to the nanometer level.

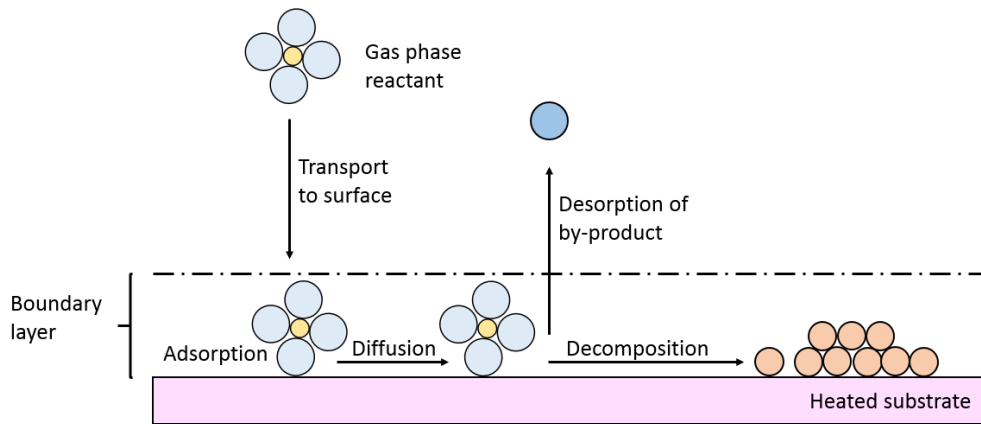


Figure 9. Schematic illustration of the CVD process.

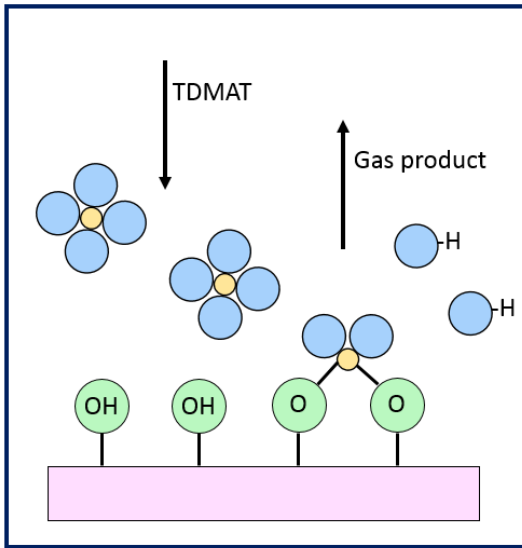
In contrast to CVD, ALD process consist of two self-limiting steps in a cycle. The ALD preparation of TiO₂ film with Tetrakis (dimethylamido) titanium (TDMAT) is illustrated in Figure 10. In the first step, TDMAT molecules are introduced by a pulse to a hydroxylated surface. When a complete monolayer of TDMAT reactant molecules have bonded to the surface, the reaction stops. Excess TDMAT molecules will be purged out of the chamber. In the second step, oxidizer molecules, which are capable of reacting with the newly formed surface, will be introduced in a pulse. A surface rich in hydroxyl groups is generated and a new layer of TiO₂ is formed. A purge of the chamber is then followed to remove the products and excess oxidizer molecules, and a cycle of ALD deposition is herein completed.

While the processing parameters continue to play a significant role in film properties, the cycling process eliminates gas phase homogenous reactions and adds a finer control on the surface reaction. Unlike what happens in CVD, incoming reactant molecules do not have to penetrate through the outgoing stream of by-products in order to reach the surface, which is the main cause of residual porosity.⁶³ With deposition monitored by cycles, layer thickness in ALD is controlled to the nanometer to sub-nanometer level.

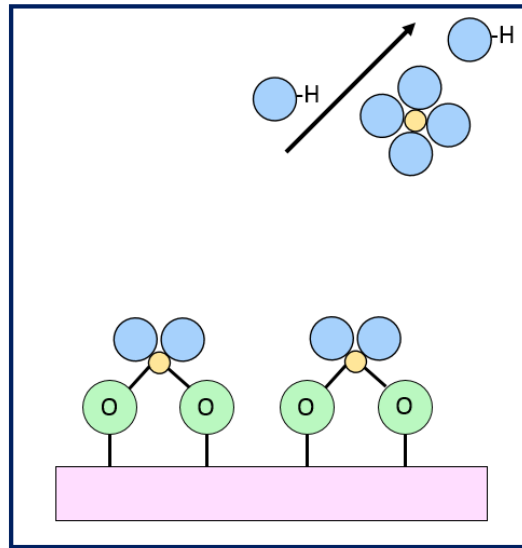
In most cases, the deposition rate is less than a monolayer of product per cycle.⁶³ There is “steric hindrance” effect associated with the precursor and there is also the gas pressure influencing adsorption equilibrium. Using the molecular volume of the precursor and the molecular volume of the deposit, we could estimate that 20% of a monolayer can be grown each cycle for our ALD TiO₂.⁶³ Using the experimental value of 0.5 Å/cycle⁶⁴⁻⁶⁵ as the growth rate with a monolayer thickness of ca. 3.5 Å for TiO₂, we could arrive at a similar value.⁶³ It is estimated that when 10 deposition cycles are repeated or when 0.5 nm of TiO₂ are deposited, a film coverage of 90% could be achieved. And when 30 deposition cycles are repeated or when 3 nm of TiO₂ are deposited, a film coverage of 100% is achieved.

STEP 1

TDMAT pulse

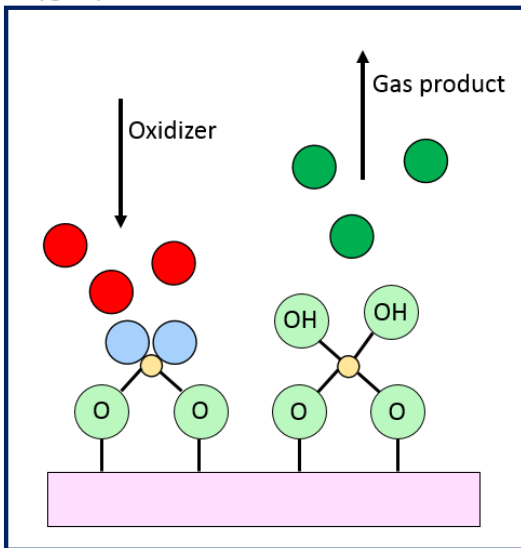


Purge



STEP 2

Oxygen pulse



Purge

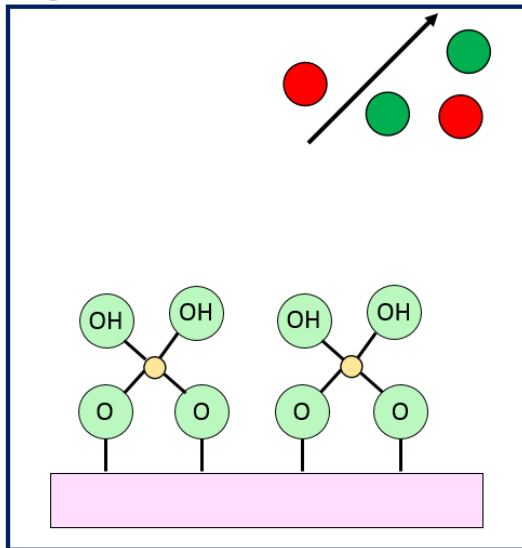


Figure 10. Schematic illustration of the ALD process.

1.3 Research Overview

Our desire is to have optimized TiO₂ films with conformal coverage and small thickness, which is critical to enhance device efficiency in OPVs by having large shunt resistance and small series resistance.

Previous work in the Armstrong group includes the development and characterization of TiO₂ films deposited by CVD as interlayers in OPVs. Kai-Lin Ou's work demonstrated that a layer of 24 nm thick CVD TiO₂ film was able to improve the OPV device by acting as an effective electron collecting / hole blocking interlayer.⁴⁸ In the precedent research, the CVD TiO₂ films were characterized by AFM/CAFM (conductive atomic force microscopy) for morphology and nanoscale conductivity features, XPS (X-ray photoelectron spectroscopy) for chemical composition, UPS (ultraviolet photoelectron spectroscopy) for frontier orbital energies, XRD (X-ray diffractometry) for molecular structure information, FE-SEM (field emission-scanning electron microscopy) for cross-sectional structure and UV-Vis (Ultraviolet–visible spectroscopy) for optical band gap. The CVD TiO₂ films were found to be amorphous, stoichiometric and conformal. CV (cyclic voltammetry) was introduced during the research as a method to probe film quality in terms of hole blocking capability.

Considering the features of CVD and ALD discussed in the last section, we have reasons to expect that TiO₂ films produced by ALD could be conformal and even thinner for OPV application.⁵⁴⁻⁵⁷ Study in Meyer's group have shown that the power conversion efficiency of dye-sensitized solar cells was dramatically increased from 0.01% to 1.10% with the addition of ALD TiO₂ from 0.6 nm to 2.4 nm.⁶⁶ They also reported an optimum ALD TiO₂ thickness of 4.5 nm for photoelectrosynthesis cell⁶⁷ and the application of 3.6 nm ALD TiO₂ in photoelectrochemical cell⁶⁸. However, the effect of ultrathin layer ALD TiO₂ film has never been demonstrated in organic photovoltaics. It is of importance and yet to be discovered how far we can go with ALD TiO₂ films of different thickness in OPVs.

Collaboration with the Graham group at Georgia Institute of Technology provided us the chance to investigate ALD TiO₂ as electron harvesting layer in organic solar cells. ALD TiO₂ films on ITOs were prepared by Hyungchul Kim in the Graham group. They measured TiO₂ film thickness using spectroscopic ellipsometry (SE). They also characterized film work function by UPS, molecular structure by XRD, and the hole blocking capability using Al/TiO₂/p-Si/Ag as testing diodes.

In this thesis, we will show our work to characterize and compare the morphology, electrical property, chemical composition and hole blocking capability of 24 nm thick CVD films and thickness varied ALD films with CAFM, XPS and CV. We will fabricate and test OPV devices and correlate device performance with film characteristics. A research background discussion is given in Chapter 1. Chapter 2 describes the experiments. Experimental results are discussed in chapter 3. Chapter 4 will summarize the work and present conclusions.

Chapter 2: Experimental

2.1 Chemical Vapor Deposition of TiO₂ Films on ITO

Indium Tin Oxide (ITO) glass substrates were purchased from Colorado Concepts Coatings LLC. Substrates were cut into 1 inch by 1 inch pieces and rinsed with water before sonication in 50% Triton X-100 detergent (Alfa-Aesar) solution. After detergent cleaning, substrates were rinsed and sonicated in water and ethanol (Decon's Pure Ethanol 200 Proof). Finally, substrates were submerged in ethanol for storing.

Before the deposition, substrates were sonicated in ethanol for 10 min and dried with nitrogen flow. They were then treated with 10.5 watts O₂ plasma at ca. 400 mTorr for 10 minutes (Harrick plasma, Model PDC-32G). Titanium (IV) isopropoxide (TTIP) (97%, Sigma-Aldrich) was used as the precursor and loaded into a glass reservoir in N₂ filled glove box.

A schematic view of the chemical vapor deposition (CVD) system is shown in Figure 11. A mass flow control (Dakota Instruments, Model 6AGC1AL4-01NC) was used to set the N₂ carrier gas flow at 0.67 sccm. N₂ gas was introduced into a reservoir and generated bubbles carrying TTIP precursor vapor. N₂ gas flow rate determines the bubbling rate of TTIP and thus the flow rate of TTIP. A tube path through a temperature controlled furnace was used to introduce the precursor to the substrate. The substrate stage is temperature controlled and the pressure is monitored. The CVD system was pumped down to ca. 500 mTorr prior to each deposition. The furnace temperature was set at 180 °C and substrate temperature at 210°C. Once deposition was finished, the substrates were allowed to cool down to ca. 90 °C in vacuum before transferring.

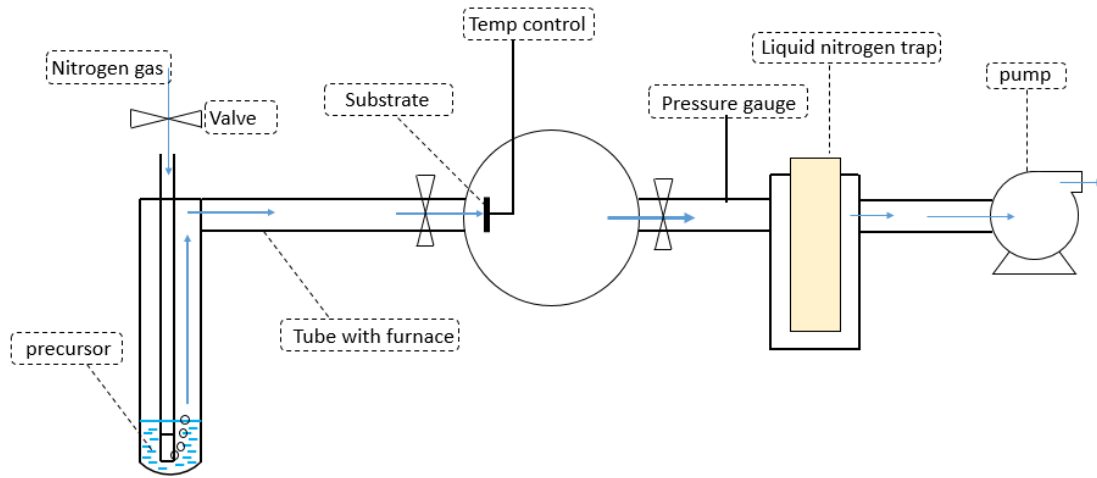


Figure 11. Schematic view of the CVD system.

2.2 Atomic Layer Deposition of TiO_2 Films on ITO

ITO/ TiO_2 samples were prepared by Hyungchul Kim in Graham's lab in Georgia Institute of Technology. Samples were transported in sealed container filled with N_2 . ITO glass substrates were from Thin Film Devices Inc. A schematic view of the atomic layer deposition (ALD) system is shown in Figure 12. For the deposition, prepared ITO substrates were placed inside the PE-ALD chamber for 10 min until temperature equilibrium was established (250°C). Tetrakis (dimethylamido) titanium (TDMAT) was pulsed into the chamber by 60 sccm of argon flow. Afterwards, the chamber was purged for 5 s. Then a remote oxygen plasma was generated at the top of the chamber with 300 W RF field on 30 sccm of oxygen flow and was delivered into the chamber by 200 sccm argon flow. The chamber was purged again for 5 s. This cycle was repeated until desired layers were deposited.

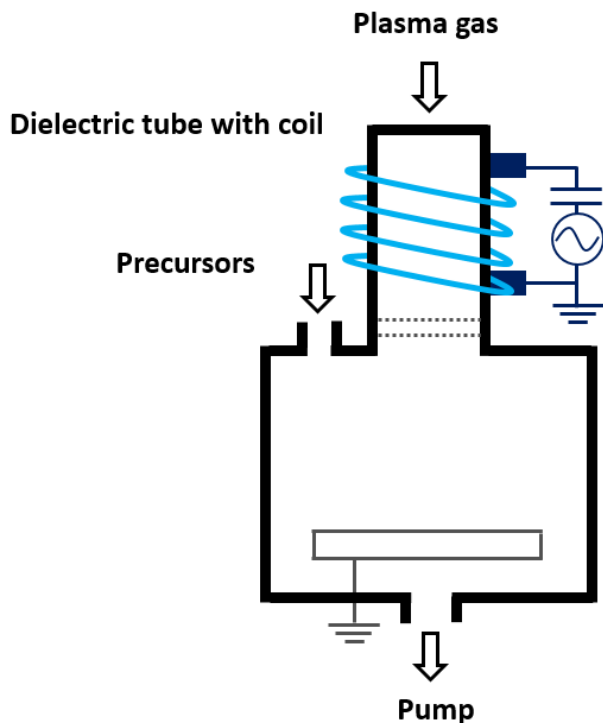


Figure 12. Schematic view the ALD system.

2.3 CAFM Characterization of Roughness, Morphology and Conductivity

Dimension 3100 AFM with a TUNA (Tunneling Atomic Force Microscopy) module (Veeco Instruments) was used for the C-AFM measurements. Measurements were all obtained in an argon-purged box environment. Conductive contact mode probes were from NanoWorld with a Platinum-iridium alloy coating (CONTPt, force constant 0.2 N/m). Samples were prepared by CVD with 24 nm thick TiO₂ films deposited on ITO glass substrates. Parallel scratches over a small area were created on TiO₂ covered samples by razor blades near and toward the edge of the substrate. The scratches revealed an area without TiO₂ covering and provided contact between ITO and silver paint (Ted Pella

Leitsilber 200). Silver paint was used to create an electrical path between ITO and the AFM instrument's sample stage. During the measurement, negative voltage biases were applied from the sample stage and the probes were held at ground.

2.4 XPS Characterization of TiO₂ Films on ITO

Kratos Axis Ultra X-ray photoelectron spectrometer was used to perform X-ray photoelectron spectroscopy (XPS). Al K α source at 1486.6 eV was used. The analyzer resolution pass energy was at 20 eV. Data were taken at normal and 60° take off angles.

2.5 Cyclic Voltammetry Characterization of ALD TiO₂ Films on ITO

Decamethylferrocene (97%, Aldrich), 1, 1-Dimethylferrocene (97%, Aldrich) and TPD (N, N'-Bis (3-methylphenyl)-N, N'-diphenylbenzidine) (99%, Aldrich) were used as probe molecules. 0.5 mM solution of each probe molecule was made in acetonitrile with 0.1 M Tetrabutylammonium hexafluorophosphate (HPLC grade, EMD). Cyclic voltammetry measurements were taken by CHI 660c potentiostat using a three port electrochemical cell with a platinum wire as counter electrode, Ag/Ag⁺ (BASi, 10 mM AgNO₃ in 0.1M TBAPF₆ electrolyte) as reference electrode and the ITO/(ALD)TiO₂ sample as working electrode (electrode area=0.671 cm²). The scan rate was 0.05 V/s.

2.6 Device Fabrication

Every 1 mL of the active layer solution was made with 20 mg of P₃HT (from Rieke Metals) and 16 mg of PC₆₁BM (from Nano-C) dissolved in 1 mL of 1, 2-dichlorobenzene (Sigma-Aldrich). The solution was kept in a nitrogen filled glove box and stirred in a capped vial at 60 °C overnight. The next day, the well mixed solution was spun on ITO/TiO₂ samples at 700 rpm for 1 min. Then the samples were let to slow dry in covered Petri dishes overnight. Then samples were annealed at 110 °C for 10 min before a PEDOT: PSS layer was spin-coated (4000 rpm, 1 min) by a PEDOT: PSS solution (Hereaus) with 1 wt% Triton X-100 (Fisher Scientific). If the PEDOT: PSS layer was not uniform after a spin coating, it was washed off with ethanol and isopropanol and then dried with N₂ flow. The spin coating is repeated until a uniform PEDOT: PSS layer is obtained. Afterwards, samples were annealed on a hot plate at 110 °C for 10 min in a nitrogen filled glove box. A 100 nm thickness Ag (99.99%, Kurt J. Lesker) contact layer was deposited by thermal evaporation at 10⁻⁶ Torr. A shadow mask was used to define a single cell area as 0.125 cm².

2.7 Device Characterization

A 300 W Xe arc lamp (Newport) was used as the light source. A neutral density filter (Thorlabs) and an AM 1.5 filter (Melles Griot) was used before the light was then passed through an optical diffuser (Newport) with a 40 degree output angle. Light intensity on device was calibrated to be 100 mW/cm² by a calibrated silicon photodiode (Newport, model 818-SL with OD3 attenuator). Potential scanning was achieved with a source meter (Keithley, model 2400) and a software (National Instruments LabView). *J-V* characteristics of the samples were measured in a nitrogen filled glove box.

Chapter 3: Results and Discussion

3.1 The Morphology and Conductivity of TiO₂ Films prepared by CVD and ALD

CAFM was used to reveal the morphology and conductivity of 24 nm thick TiO₂ film deposited by chemical vapor deposition (CVD) on ITO (Colorado Concepts Coatings LLC) substrate.

Comparing the height images of bare ITO (Figure 13c) and ITO/(CVD 24 nm)TiO₂ (Figure 13a), the sub-grain features of ITO remains visible after the deposition of 24 nm TiO₂ film. And there is only a slight change in root-mean-square (rms) surface roughness from 2.7 nm measured for bare ITO to 3.0 nm measured for ITO/(CVD 24 nm)TiO₂. The histograms of the height images show that height distributions are similar for the two samples. Thus the height images suggest that conformal TiO₂ films were deposited by CVD on ITO, which is in agreement with previous studies in the group and being conformal is an important character to indicate pinhole-free films with no excessive amount of resistive grain boundaries.⁴⁸

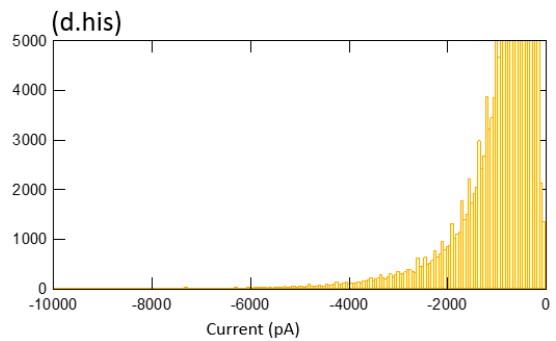
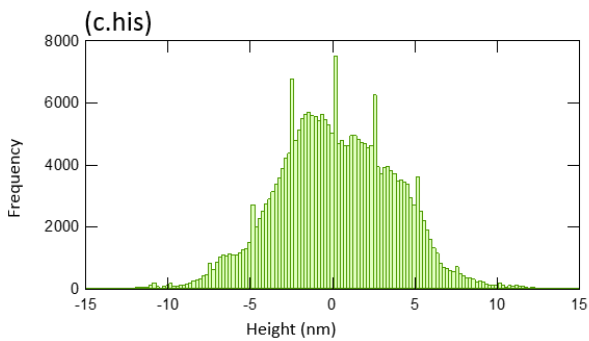
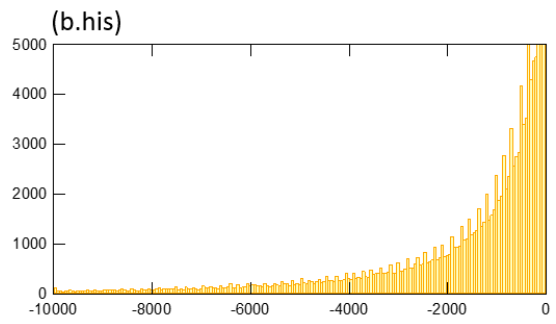
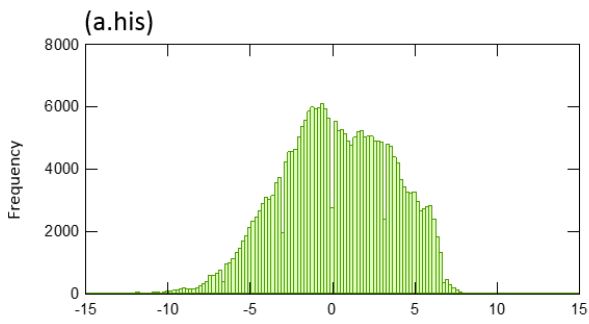
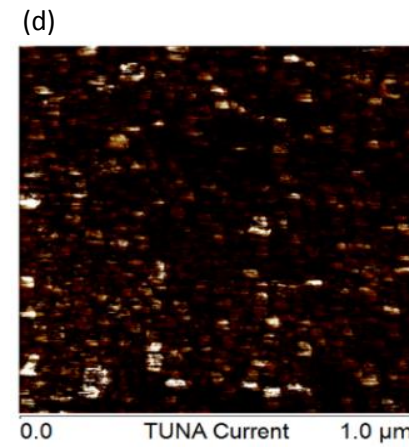
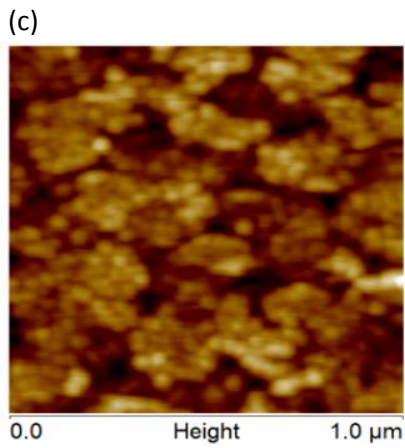
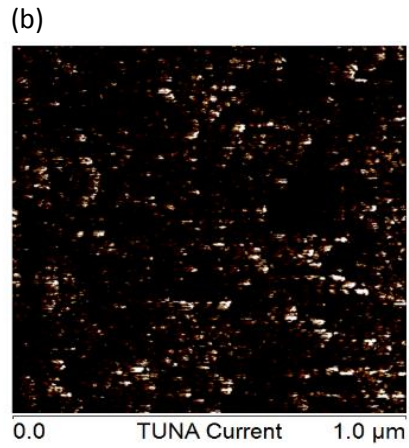
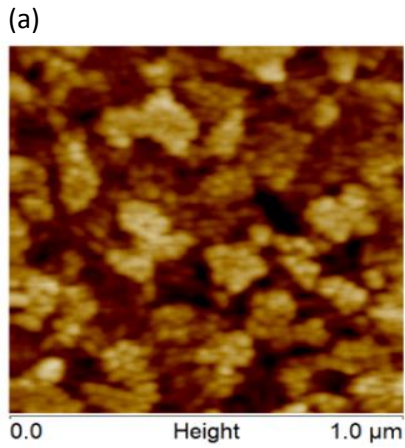


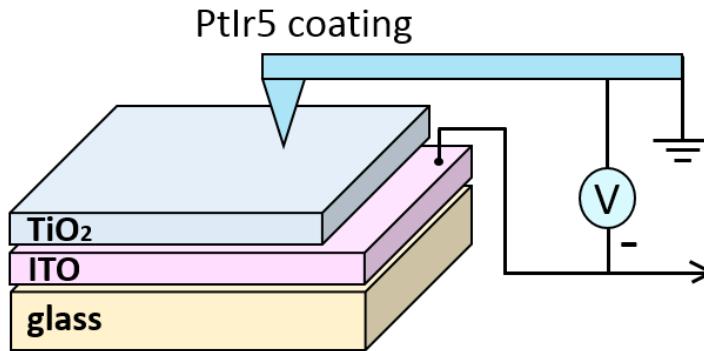
Figure 13. Contact mode CAFM images and associated histograms of bare ITO and ITO/TiO₂ samples. (a) Height image of bare ITO. (b) Current image of bare ITO at -0.100 V bias. (c) Height image of ITO/(CVD 24 nm)TiO₂. (d) Current image of ITO/(CVD 24 nm)TiO₂ at -4.000 V bias. (a.his) Associated histogram of image a with bin size of 0.2 nm. (b.his) Associated histogram of image b with a bin size of 50 pA. (c.his) Associated histogram of image c with bin size of 0.2 nm. (d.his) Associated histogram of image d with a bin size of 50 pA.

Figure 14 shows the experimental schematic diagram of CAFM measurements and pre-contact energy levels of materials used in measurement. Current data is obtained with a constant negative bias held at the sample stage, which is connected to the ITO layer via silver paint. In the measurement process, electrons are transported from the ITO through the TiO₂ layer to the probe. At a same bias, a higher average current magnitude would indicate a more conductive sample. The differences presented in current magnitudes are a result of electron transport at the ITO/TiO₂ interface, in the TiO₂ film layer and at the TiO₂/probe interface. The direction at which the electrons flow in CAFM measurement is the same as the direction electrons flow in a leakage current in the photovoltaic devices presented later.

Figure 13 contains the current images of ITO/TiO₂ samples. There is a significant difference in conductivity between the samples with and without 24 nm TiO₂ layer, while the histograms show similar current distributions. The current image of bare ITO was obtained at -0.100 V bias and revealed an average current of 3.4 ± 0.3 nA, while the current image of ITO/(CVD 24 nm)TiO₂ was obtained at -4.000 V bias and revealed an average current of 0.8 ± 0.08 nA. At -0.100 V the ITO/(CVD 24 nm)TiO₂ sample wasn't able to exhibit detectable amount of current. Therefore, the two samples were held at

different biases to reveal suitable amount of measurable current. Though applied with higher bias, ITO/(CVD 24 nm)TiO₂ sample showed significantly smaller average current. In other words, the ITO sample with 24 nm of TiO₂ deposited by CVD is effective in obstructing electron flow in the direction that is associated with leakage current in the photovoltaic devices. This agrees with the results reported by Ou et al.,⁴⁸ where the leakage current of photovoltaic devices with bare ITO is substantially higher than those with ITO/(CVD)TiO₂.

(a)



(b)

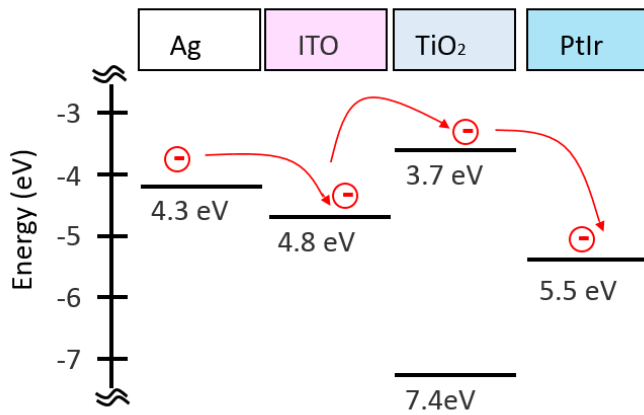


Figure 14. (a) Schematic diagram of CAFM measurements and proposed (b) pre-contact energy levels of materials used in measurement.

CAFM was used to explore the morphology and conductivity of ITO (Thin Film Devices, Inc) substrates covered with TiO₂ films of different thicknesses deposited by atomic layer deposition (ALD).

The height images and associated histograms of four samples, bare ITO, ITO/(ALD 1 nm)TiO₂, ITO/(ALD 3 nm)TiO₂, and ITO/(ALD 10 nm)TiO₂ are shown in Figure 15. They exhibit no visual difference from each other. The rms surface roughness, summarized in table 1, for all samples is 0.4 nm. The indistinguishable differences in morphology and roughness among samples suggest that conformal TiO₂ films were deposited by ALD for all thicknesses.

The histogram of the height image of sample with 0.5 nm TiO₂ deposited shows wider height distribution compared to that of the bare ITO, and as the TiO₂ film thickness gets thicker, the height distribution gets smaller. This could suggest a reorganization of the deposit during the deposition process.

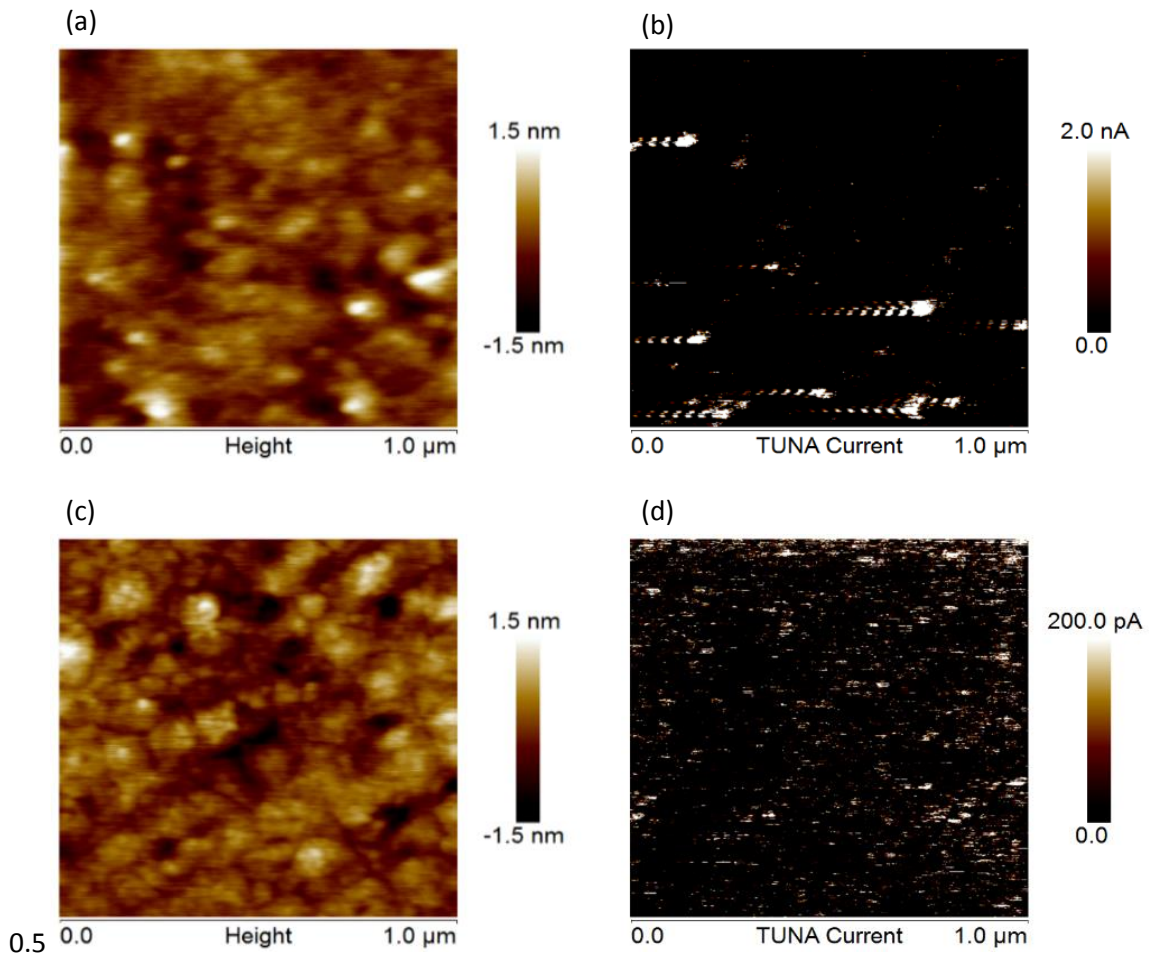
The applied bias and respective average currents are summarized in Table 1. Comparing the CAFM results between bare ITO and ITO/(ALD 1 nm)TiO₂, the average current magnitude decreased from 3.8 ± 0.4 to 0.15 ± 0.02 nA as TiO₂ is deposited, even though ITO/(ALD 1 nm)TiO₂ was under higher bias. The average current magnitude decreased from 0.15 ± 0.02 nA (at -2.000 V) to 0.02 ± 0.003 nA (at -2.000 V) as TiO₂ thickness increased from 1 nm to 3 nm. However, the average current magnitude increased from 0.02 ± 0.003 nA (at -2.000 V) to 0.29 ± 0.03 nA (at -1.500 V), when the film thickness increased from 3 nm to 10 nm.

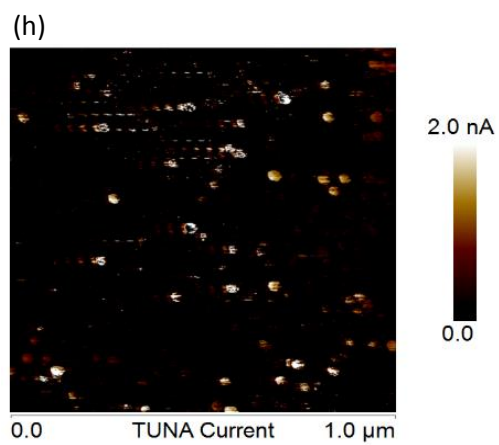
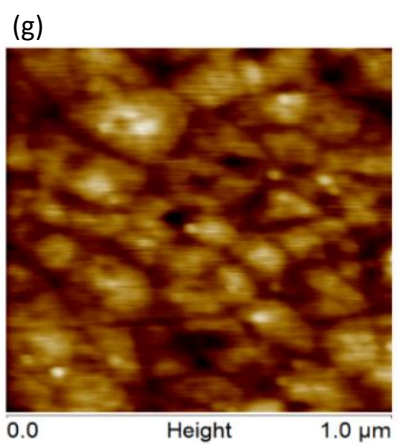
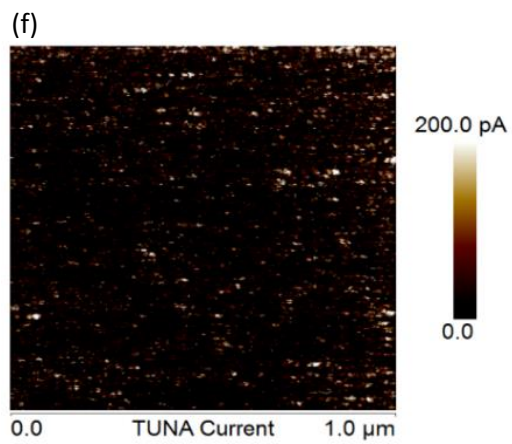
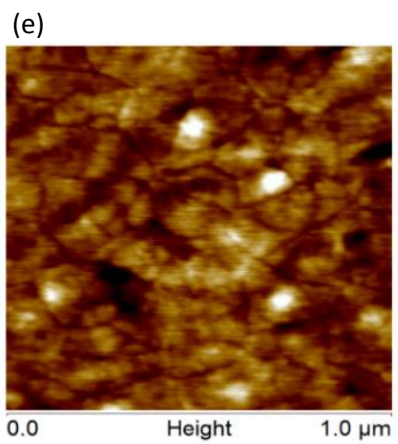
For the sample with 10 nm TiO₂, the current image and its associated histograms in Figure 15 shows localized hot spots for current flow, which is associated the higher height features in the height image. The average current increase is a result of both these hot spots and the overall increase in conductivity accompanied by wider current distribution, larger sigma (Table 1). The sudden appearance of these hot spots and the change in overall conductivity of the ITO/(ALD 10 nm)TiO₂ sample is considered to be related to the phase change of deposited TiO₂. The evidence is given in Figure 16, where we see the GIXRD patterns of 10 nm and 5 nm TiO₂ films deposited on Si substrate. This figure is provided by the Graham group at Georgia Institute of Technology. It shows that the 5 nm TiO₂ film exhibits no clear diffraction peaks, which means it is amorphous. Meanwhile the 10 nm TiO₂ film exhibits peaks that overlap with those of anatase TiO₂, meaning the film is anatase. The phase change of ALD TiO₂ from amorphous to anatase as film thickness increases is also observed in other studies.⁶⁹⁻⁷² Researchers have shown that anatase TiO₂ is more conductive than amorphous TiO₂.⁷³⁻⁷⁴

Sample ITO/(ALD 3 nm)TiO₂ is the least conductive sample among all ITO/(ALD)TiO₂ samples, and it is predicted to create photovoltaic devices with the least amount of leakage current and largest value of shunt resistance. This is confirmed by the results presented in Table 4 and Figure 20a.

In summary, TiO₂ films deposited by both CVD and ALD exhibited conformal coverage. And this is considered to be the first sign to indicate pinhole-free films. Being unable to hold all substrates at the same bias for the CAFM measurements, it is hard to compare conductivity across all samples. But it is clear that ITO/(ALD)TiO₂ sample conductivity decreases with film thickness increasing from 1 nm to 3 nm, and increases with film

thickness increasing from 3 nm to 10 nm. ITO/(ALD 3 nm)TiO₂ exhibited the lowest conductivity among all along ITO/(ALD)TiO₂ samples, which is in agreement with its least amount of leakage current and shunt resistance among all ITO/(ALD)TiO₂ devices. ITO/(CVD 24 nm)TiO₂ exhibited the lowest conductivity among all ITO/TiO₂ samples in congruence with its smallest leakage current and largest shunt resistance among all devices. It is a surprise and an achievement that such thin 0.5 nm to 10 nm thick of ALD TiO₂ films were able to reduce the measured average current to ca. 1/10 of the original, which is comparable to the effect of 24 nm CVD TiO₂.





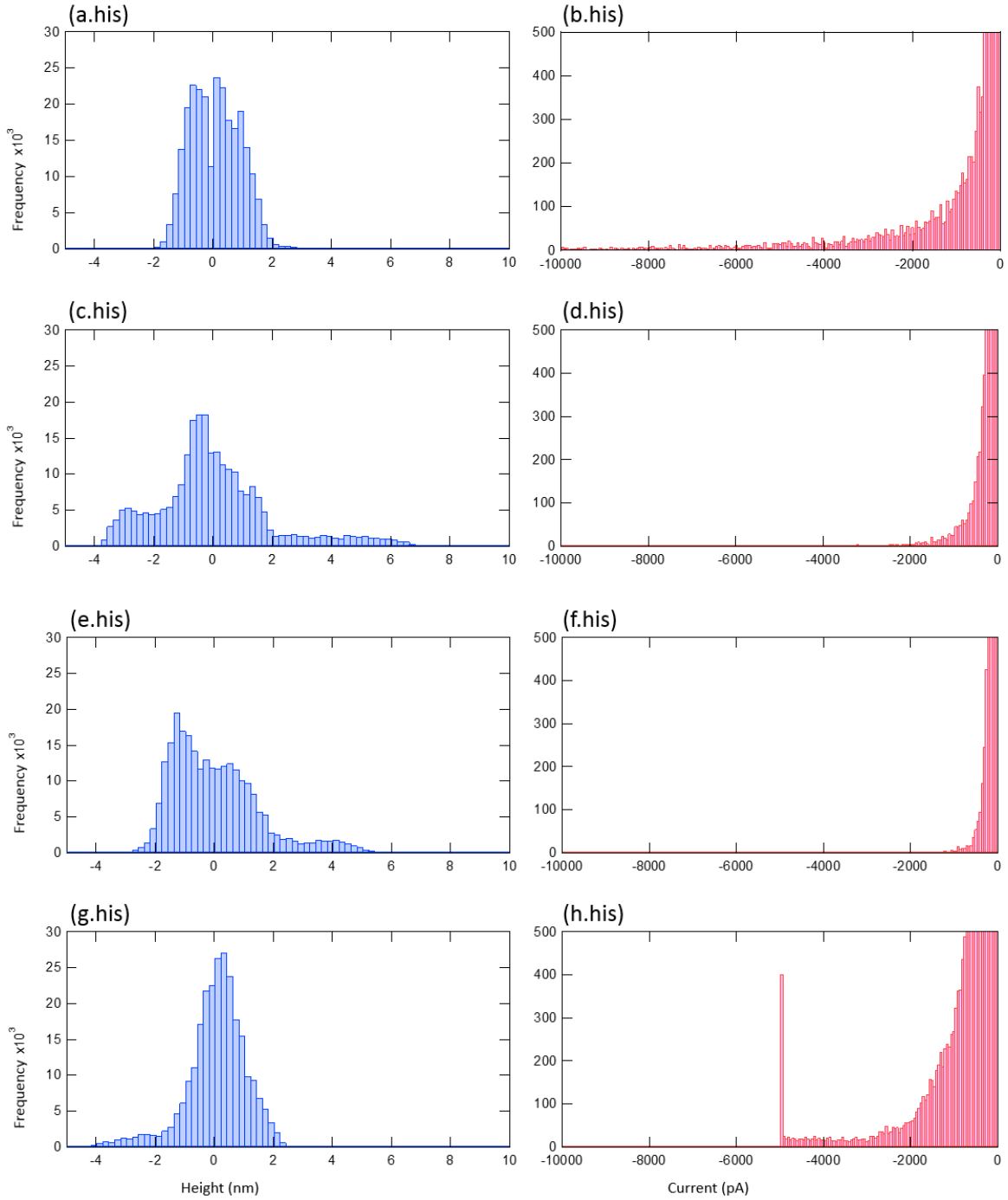


Figure 15. Contact mode CAFM images and associated histograms of bare ITO and ITO/TiO₂ samples. (a) Height image of bare ITO. (b) Current image of bare ITO at -1.000 V bias. (c) Height image of ITO/(ALD 1 nm)TiO₂. (d) Current image of ITO/(ALD 1 nm)TiO₂ at -2.000 V bias. (e) Height image of ITO/(ALD 3 nm)TiO₂. (f) Current image of ITO/(ALD 3 nm)TiO₂ at -2.000 V bias. (g) Height image of ITO/(ALD 10 nm)TiO₂. (h) Current image of ITO/(ALD 10 nm)TiO₂ at -1.500 V bias. (a.his) Associated histogram of

image a with bin size of 0.2 nm. (b.his) Associated histogram of image b with a bin size of 50 pA. (c.his) Associated histogram of image c with bin size of 0.2 nm. (d.his) Associated histogram of image d with a bin size of 50 pA. (e.his) Associated histogram of image e with bin size of 0.2 nm. (f.his) Associated histogram of image f with a bin size of 50 pA. (g.his) Associated histogram of image g with bin size of 0.2 nm. (h.his) Associated histogram of image h with a bin size of 50 pA.

Table 1. Summary of Contact mode CAFM results. Sigma is obtained assuming the current distribution is Gaussian.

Sample name	Rms roughness (nm)	Bias (V)	Average current (nA)	Sigma (pA)
TFD-ITO	0.4	-1.000	3.8 ± 0.4	0.93
TFD-ITO/(ALD 1 nm)TiO₂	0.4	-2.000	0.15 ± 0.02	0.50
TFD-ITO/(ALD 3 nm)TiO₂	0.4	-2.000	0.02 ± 0.003	0.44
TFD-ITO/(ALD 10 nm)TiO₂	0.4	-1.500	0.29 ± 0.03	0.63
CC-ITO	2.7	-0.100	3.4 ± 0.3	12.2
CC-ITO/(CVD 24 nm)TiO₂	3.0	-4.000	0.8 ± 0.08	8.0

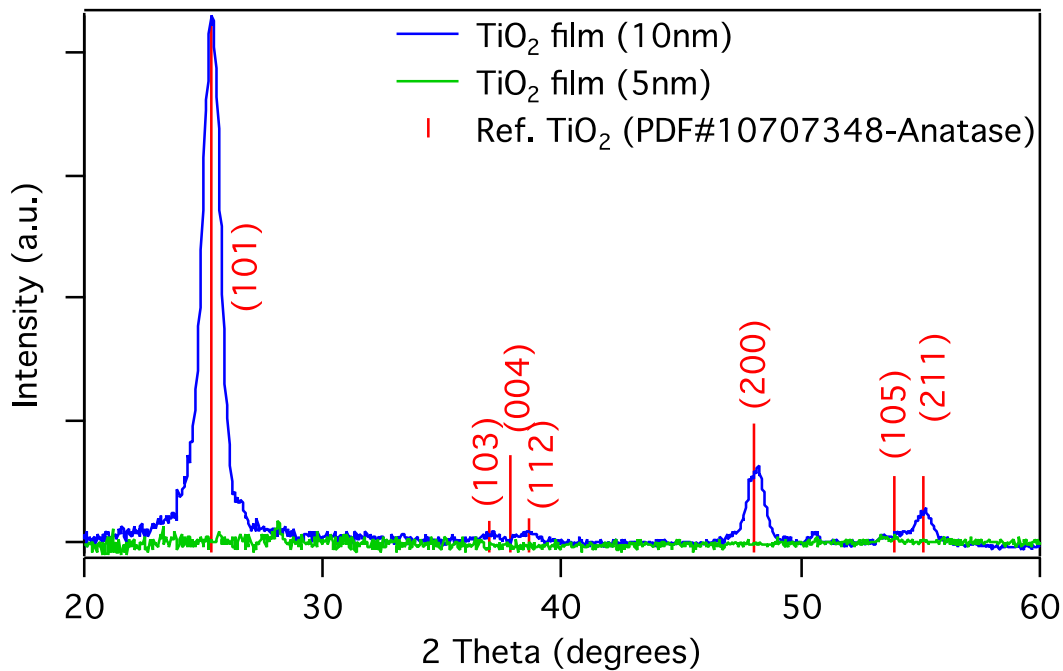


Figure 16. GIXRD patterns of a 10 nm (blue line) and 5 nm (green line) TiO₂ films deposited on Si with 0.18° incidence angle. The red lines give the XRD pattern of reference anatase TiO₂ (PDF 01-070-7348). Image is provided by the Graham group at Georgia Institute of Technology.

3.2 ITO/TiO₂ Surface Composition (XPS)

X-ray photoelectron spectroscopy (XPS) was used to reveal the surface composition and chemical states of ITO/TiO₂ substrates.

Figure 17 shows the XPS results of Ti 2p peaks for four different ITO/TiO₂ samples. The handbook value of the binding energy of Ti 2p_{3/2} peak in TiO₂ is 458.5 eV with a spin-orbit splitting of 5.7 eV. And it is also known from previous studies that the binding energy difference between O 1s and Ti 2p_{3/2} (Δ BE) is 71.5 ± 0.2 eV in TiO₂.⁷⁵ The binding energy results for Ti 2p peaks summarized in Table 2 agree with the binding energy characteristics

for TiO_2 discussed above. It is thus concluded that our samples prepared by both CVD and ALD are carrying stoichiometric TiO_2 films. The symmetry of Ti 2p peaks and the absence of any shoulder bands are also a demonstration of the lack of lower valence states of titanium, such as Ti^{3+} , Ti^{2+} , etc.⁷⁶

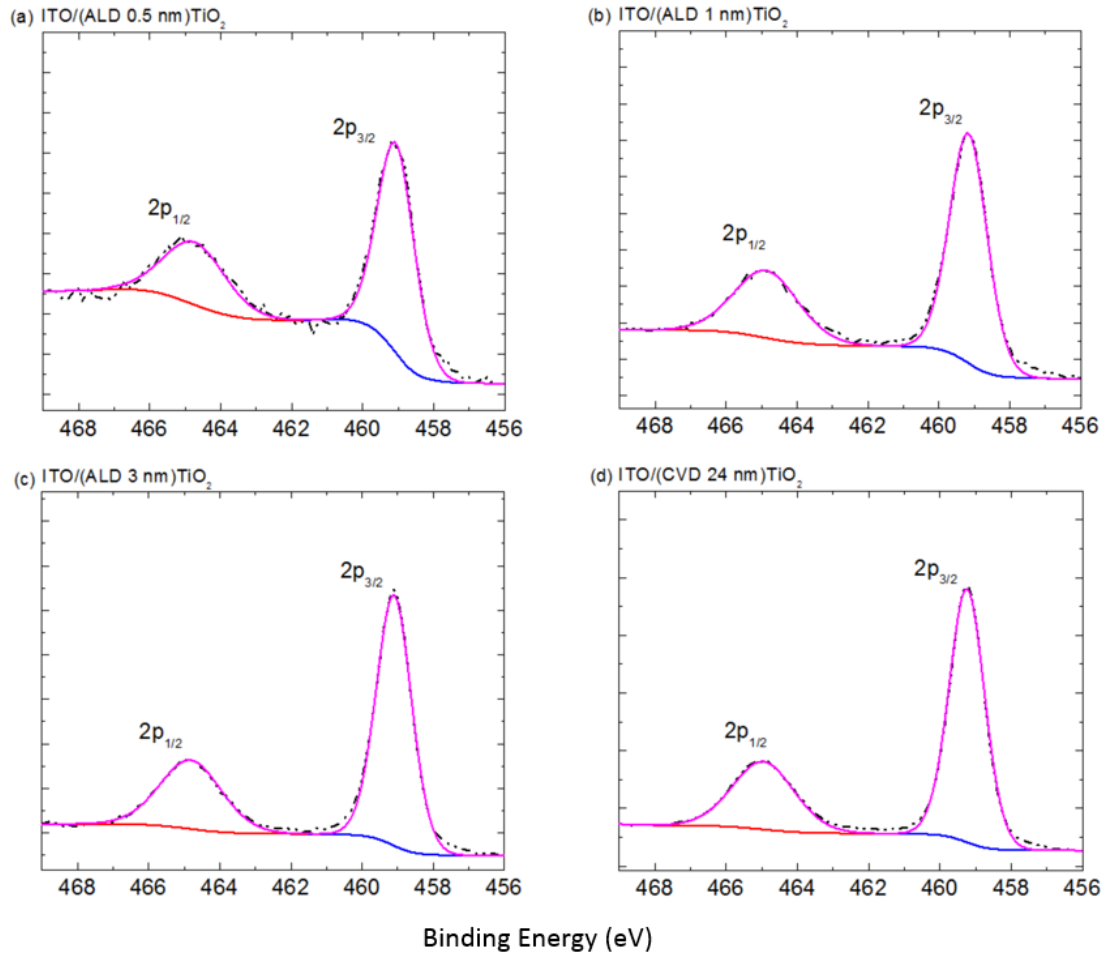


Figure 17. Ti 2p XPS spectra for ITO/ TiO_2 samples. (a) ITO/(ALD 0.5 nm) TiO_2 , (b) ITO/(ALD 1 nm) TiO_2 , (c) ITO/(ALD 3 nm) TiO_2 , (d) ITO/(CVD 24 nm) TiO_2 .

Table 2. Summary of analysis of binding energy results from XPS for Ti 2p peaks.

sample	Ti 2p _{3/2} peak binding energy (eV)	Ti 2p _{3/2} peak FWHM (eV)	Ti 2p spin-orbit splitting (eV)	ΔBE between Ti 2p _{3/2} and O 1s (eV)
ITO/(ALD 0.5 nm)TiO ₂	458.4	1.2	5.6	71.4
ITO/(ALD 1 nm)TiO ₂	458.4	1.2	5.7	71.5
ITO/(ALD 3 nm)TiO ₂	458.5	1.1	5.7	71.5
ITO/(CVD 24 nm)TiO ₂	458.5	1.1	5.7	71.5

Figure 18 and Figure 19 show In 3d and O 1s spectra respectively for ITO/(ALD)TiO₂ samples with different thicknesses measured at 0° and 60° takeoff angle. Indium was observed for all ITO/(ALD)TiO₂ samples in the XPS spectra, which is an indication that the O²⁻ component in O 1s peak has two sources, TiO₂ and ITO. The lattice O²⁻ from TiO₂ and ITO cannot be distinguished. This explains why the computed lattice O²⁻ to Ti composition ratios for ITO/(ALD)TiO₂ samples are above two and change with film thickness and takeoff angle. Therefore, it would not be feasible to use this composition ratio to represent oxygen to titanium ratio in ALD TiO₂ film layers. Indium was not observed for ITO/(CVD 24 nm)TiO₂ samples. The computed lattice O²⁻ to Ti composition ratio for ITO/(CVD 24 nm)TiO₂ samples is 2.08, which represents a stoichiometric TiO₂ film.

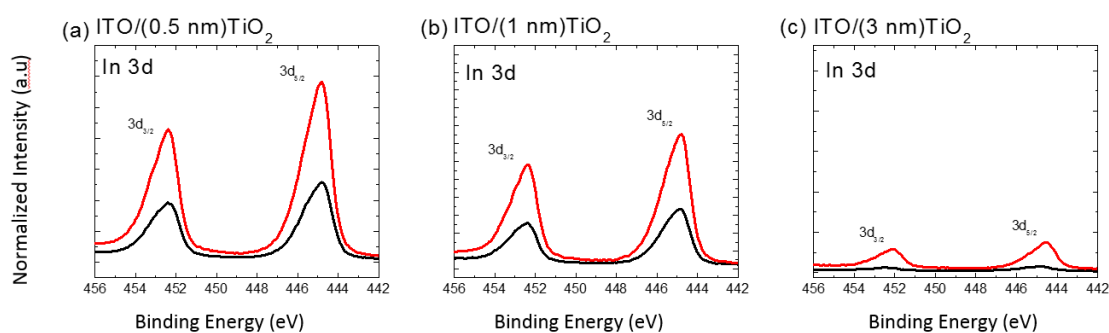


Figure 18. In 3d XPS spectra for ITO/TiO₂ samples. (a) ITO/(ALD 0.5 nm)TiO₂, (b) ITO/(ALD 1 nm)TiO₂, (c) ITO/(ALD 3 nm)TiO₂. Measurements were taken at 0° (red dashed lines) and 60° (black dashed lines) take-off angles for each sample.

The O 1s peak has three components: oxide oxygen at 530.0 eV, hydroxyl oxygen at 531.3 eV and oxygen from carbon contamination species at 532.3 eV.^{2, 48, 77} The results are presented in Figure 19 and Table 3. At both measurement angles, there is a lower % composition of hydroxyl oxygen when the ALD TiO₂ film is thicker. The higher oxide density of TiO₂ film than ITO will contribute to this change and thus it is not clear whether the thicker film contains less or more hydroxyl oxygen. As measurement angle is tilted from 0° to 60°, surface sensitivity is enhanced. It is observed that In 3d peak diminishes as the film thickness increases and as the take-off angle is increased. This stands by the fact that the ITO lies beneath the TiO₂ layer. The % composition of hydroxyl oxygen is increased when take-off is increased. This indicates that hydroxyl is richer in the near surface region. Because the XPS measurement was able to sample through the whole ALD TiO₂ layer at both takeoff angles, it is not clear from this observation whether the detected hydroxyl oxygens reside beneath, within or above the ALD TiO₂ layer. But we know that

the last step in the ALD cycle oxygen was introduced to the TiO₂ surface, which should in turn produce a Ti-OH surface species. So likely hydroxyl groups are rich on the top surface. And it is known that residue physisorbed water are common sources of surface hydroxyl oxygen for samples that were once exposed to atmosphere.⁷⁸ Both the underneath ITO surface and the top TiO₂ surface are susceptible to this source of hydroxyl oxygen.⁷⁹⁻⁸⁰ Former studies have shown that Ti-OH defects (hydroxyl residing within the TiO₂ film) would introduce electronic levels within the band gap of TiO₂ by creating lattice distortion and thus increase electron conductivity of the film.^{78, 81-83} The decreasing series resistance with increasing film thickness observed in device characterization containing ALD TiO₂ film discussed later suggests that there might be Ti-OH defect lying within the ALD TiO₂ film.

In summary, Ti⁴⁺ is proved as the chemical state of Ti in both CVD and ALD TiO₂ films. For ITO/(ALD)TiO₂ of all thicknesses, angle resolved XPS results show that there is a higher % composition of hydroxyl oxygen in the near surface region. While there are reasons to believe that hydroxyl oxygens reside on both ITO and TiO₂ surfaces, there is no reason to rule out that hydroxyl oxygens also reside within the TiO₂ film. TiO₂ films containing Ti-OH defects are more conductive,^{78, 81-83} which could correlate with decreased series resistance. A more hydrophilic TiO₂ surface would favor a better vertical phase separation of the heterojunction layer, which is more electron transporting PCMB is on the bottom⁸⁴.

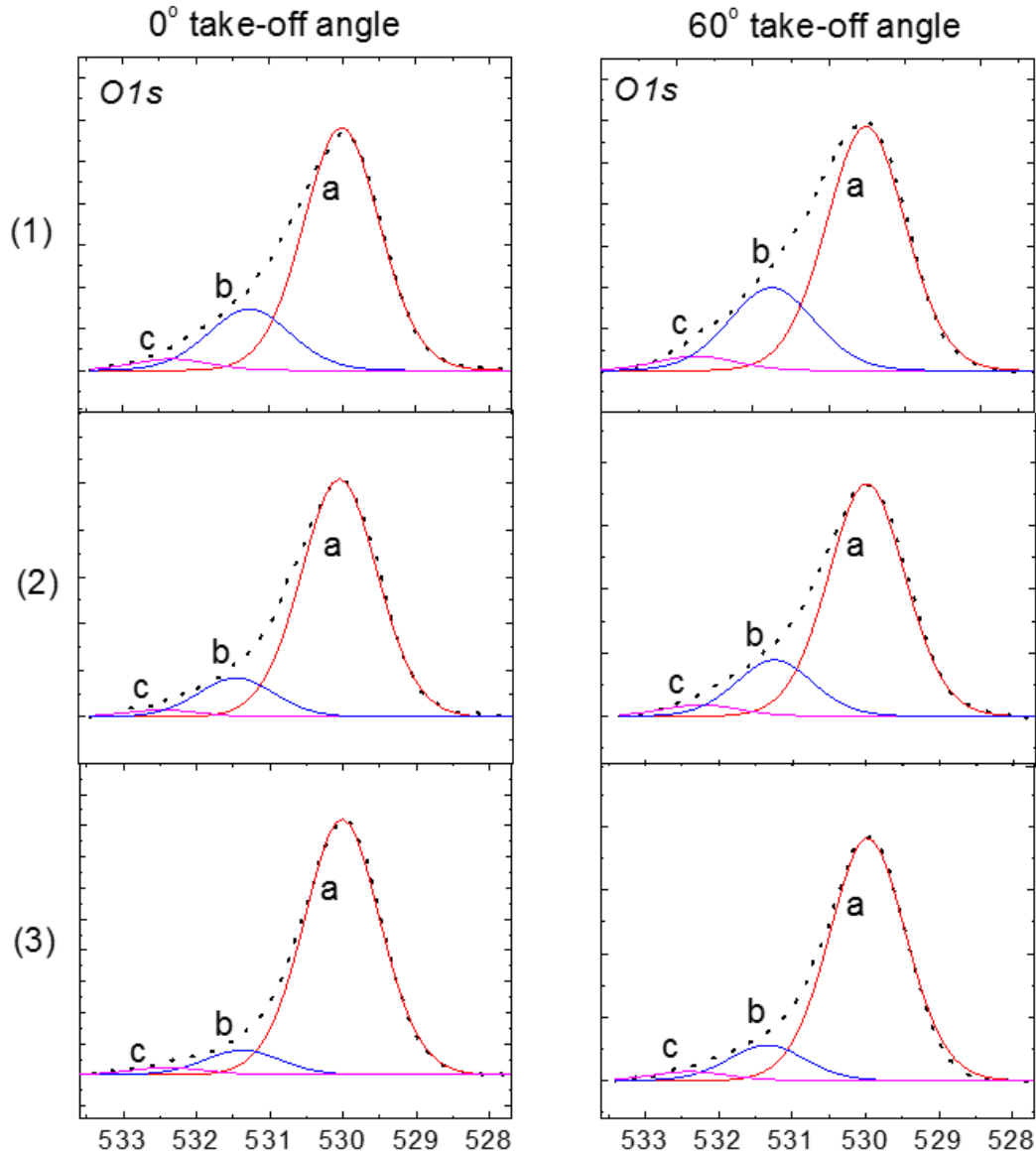


Figure 19. O 1s XPS spectra for ITO/TiO₂ samples. (1) ITO/(ALD 0.5 nm)TiO₂, (2) ITO/(ALD 1 nm)TiO₂, (3) ITO/(ALD 3 nm)TiO₂. O 1s component 'a' at 530.0 eV is attributed to TiO₂ and ITO O²⁻. O 1s component 'b' at 531.3 eV is attributed to the hydroxyl group. O 1s component 'c' at 532.3 eV is attributed to C-O.

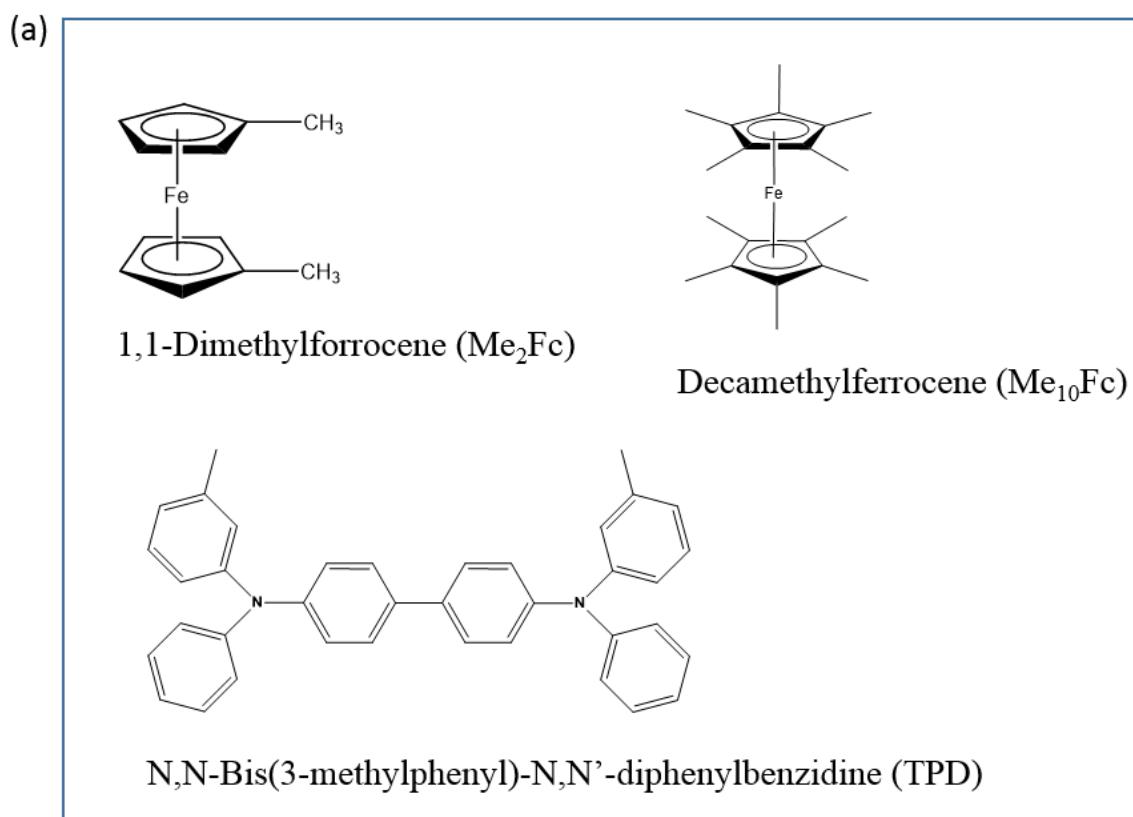
Table 3. % composition of O 1s components from XPS thickness varied ITO/TiO₂ samples.

take-off angle	TiO ₂ thickness (nm)	% composition of oxide O 1s	% composition of hydroxyl O 1s	% composition of C-O O 1s	Lattice O ²⁻ to Ti ratio
0°	0.5	75.8 ±0.3	20.7 ±0.1	3.5 ±0.1	5.33
	1	83.8 ±0.3	13.8 ±0.1	2.4 ±0.1	3.49
	3	88.8 ±0.3	8.6 ±0.1	2.6 ±0.1	2.40
	24	85.2 ±0.3	12.0 ±0.1	2.8 ±0.1	2.08
60°	0.5	70.1 ±0.3	25.7 ±0.1	4.1 ±0.1	3.85
	1	77.6 ±0.3	18.7 ±0.1	3.7 ±0.1	2.44
	3	84.6 ±0.3	12.4 ±0.1	3.0 ±0.1	2.05

3.3 Charge Blocking Behavior (CV)

Electrochemical probe molecules with their reduction potentials lying within the band gap of TiO₂ were used to evaluate the charge blocking capability of TiO₂ films.^{48, 85} It was reported that ITO/(CVD 24 nm)TiO₂ electrodes were able to block the electrochemical activity of probe molecules such as ferrocene (Fc/Fc⁺) and N, N'-Bis (3-methylphenyl)-N, N'-diphenylbenzidine (TPD) substantially. In this experiment, three probes molecules, 1,1-Dimethylferrocene (Me₂Fc), Decamethylferrocene (Me₁₀Fc) and N,N-Bis(3-

methylphenyl)-N,N'-diphenylbenzidine (TPD), whose reduction potentials lie within the band gap of TiO₂, were chosen to study the charge blocking capability of ALD TiO₂ films. Figure 20 gives the structure of probe molecules and an illustration of TiO₂ blocking electrochemical activity of probe molecules.



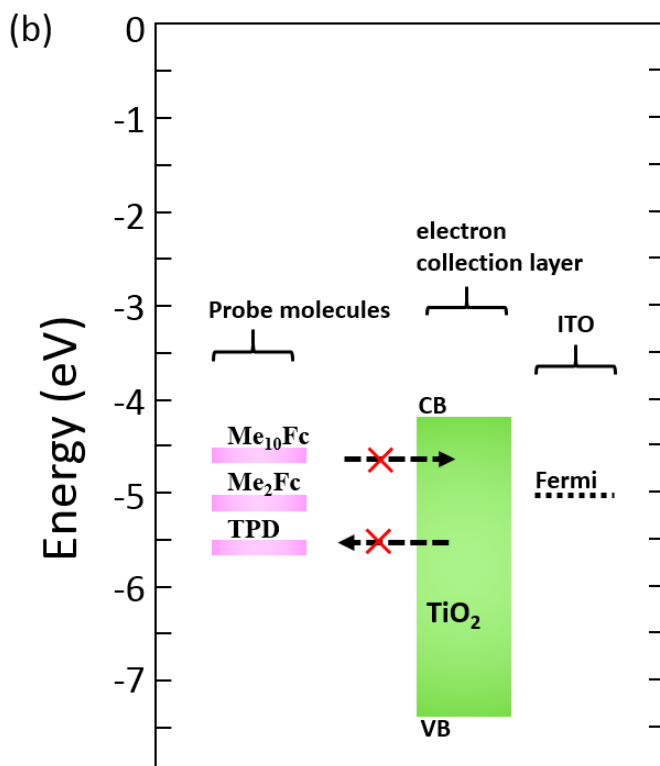
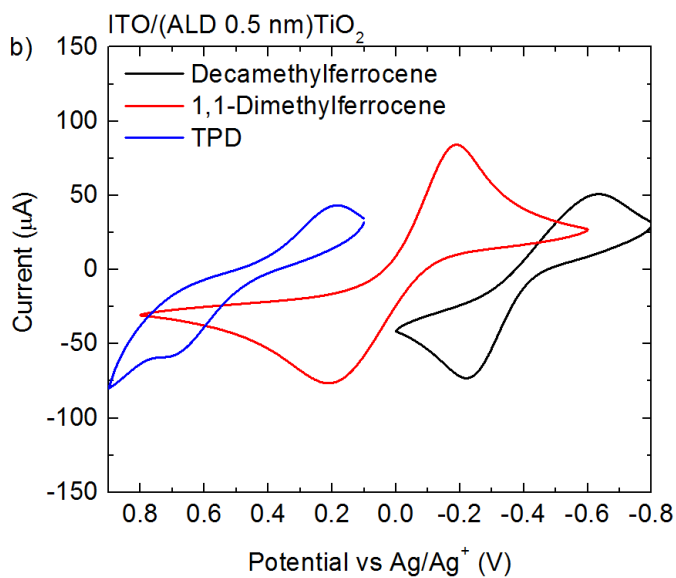
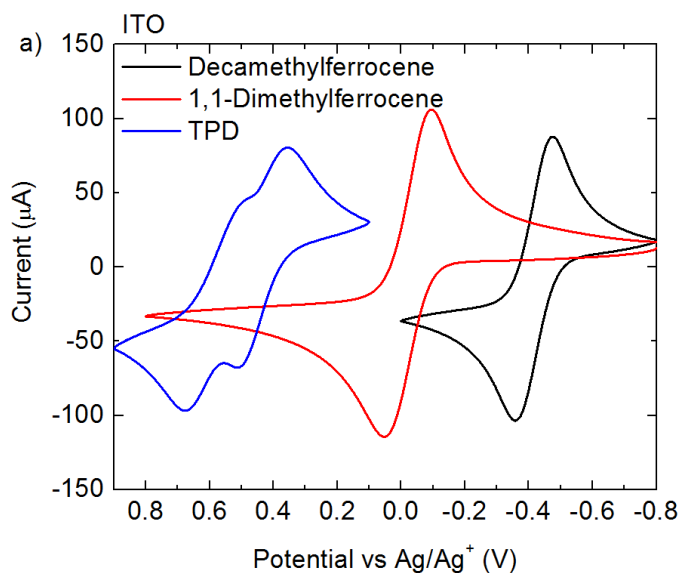
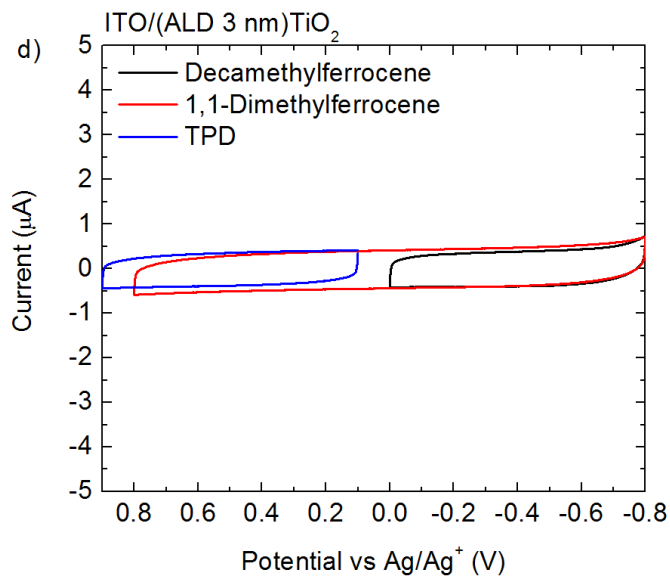
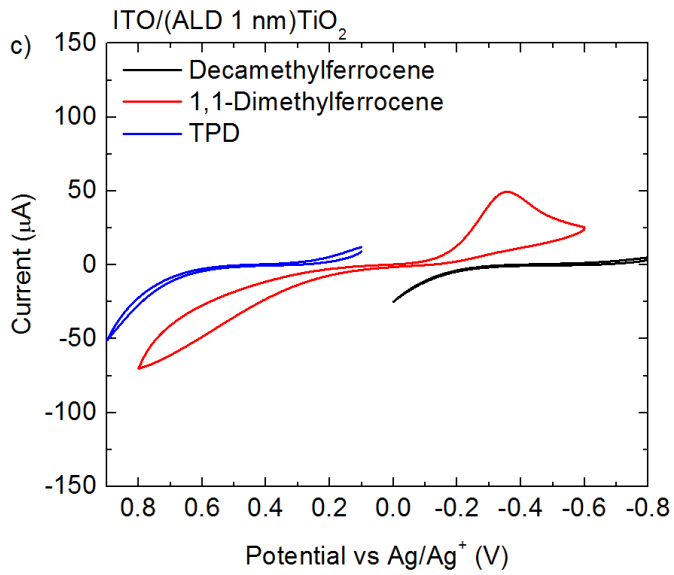


Figure 20. (a) Electrochemical probe molecules. (b) Illustration of TiO₂ blocking electrochemical activity of probe molecules.

Figure 21a shows the cyclic voltammetry results for all three probe molecules with bare ITO. The reduction/oxidation processes of these molecules were demonstrated by the reductive/oxidative waves on the cyclic voltammogram. Figure 21 b, c, d, and e are the voltammograms of probe molecules with ITO/(ALD)TiO₂ electrodes as the thickness of TiO₂ film increases. The current density magnitude of redox waves decreases as the film thickness is increased from 0.5 nm to 1 nm, and it is accompanied by a significant loss in wave symmetry. A decrease in the magnitude of the current is an indication of improved surface coverage with less pin holes⁸⁵. With 3 or 10 nm thick TiO₂, the rectangular shaped voltammograms indicate that only non-faradaic events are allowed. This is a demonstration

that 3 nm and 10 nm ALD TiO₂ films are effectively blocking charge transfer events in its band gap region, which means these films have a low density of gap states (being stoichiometric) and are uniformly deposited (being free of pin holes). These results are consistent with findings in CAFM and XPS experiments.





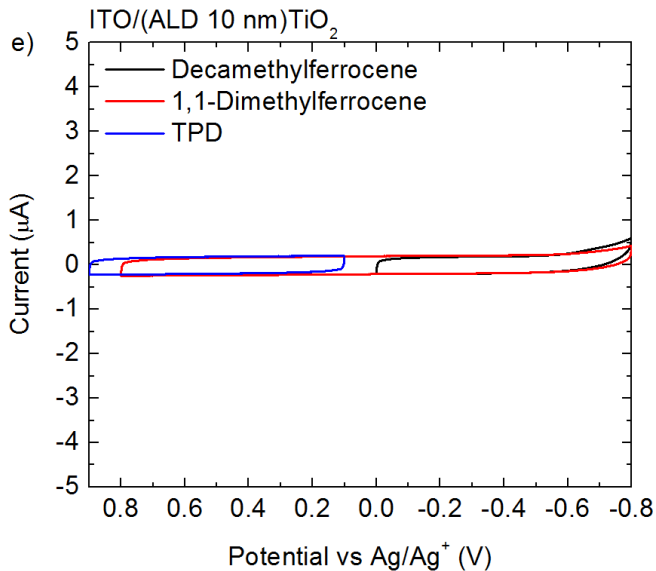


Figure 21. Cyclic voltammograms of probe molecules Decamethylferrocene, 1,1-Dimethylferrocene, and TPD(N,N'-Bis(3-methylphenyl)-N,N'-diphenylbenzidine) with a) bare ITO electrode, b) ITO/(ALD 0.5 nm)TiO₂, c) ITO/(ALD 1 nm)TiO₂, d) ITO/(ALD 3 nm)TiO₂, e) ITO/(ALD 10 nm)TiO₂. The potential was scanned at 0.05 V/s vs Ag/Ag⁺ reference electrode.

The heterogeneous electron transfer rate constant (k_s) of dimethylferrocene can be estimated from its peak separation. Values of peak separation are obtained from the voltammograms of 1,1-dimethylferrocene. The value of charge transfer parameter (φ) can be determined from the value of peak separation (ΔE_p) by former experimental results.⁸⁶⁻⁸⁷ The relationship between the charge transfer parameter (φ) and the heterogeneous electron transfer rate constant (k_s) is given by the equation⁸⁶ below:

$$\varphi = \gamma^\alpha k_s / \sqrt{\pi a D_o} \quad (\text{Equation 5})$$

where D_o is the diffusion coefficient of oxidized species and D_R is the diffusion coefficient of reduced species; Assume $D_o = D_R$ then $\gamma = \left(\frac{D_o}{D_R}\right)^{1/2} = 1$; the value of D_o for

dimethylferrocene is estimated from literature⁸⁸ as $1.35 \times 10^{-7} \text{ cm}^2/\text{s}$; the charge transfer coefficient (α) is assumed to be 0.5; $a = nFv/RT$, where $n = 1$, $F = 96485 \text{ C/mol}$, $v = 0.05 \text{ V/s}$, $R = 8.314 \frac{\text{J}}{\text{mol}\cdot\text{K}}$, $T = 298 \text{ K}$. With calculation, k_s of dimethylferrocene (DMFc) in acetonitrile using Tetrabutylammonium hexafluorophosphate (NBu_4PF_6) as the supporting electrolyte are estimated. The results are summarized in table 4.

If we assume that electrons transfer through the TiO_2 layer by tunneling, the rate of electron transfer with $\text{ITO}/(\text{ALD } 0.5 \text{ nm})\text{TiO}_2$ can be predicted from that with bare ITO. The electron tunneling decreases exponentially with increasing distance (d):⁸⁹⁻⁹⁰

$$k'_s = k_s \exp(-\beta d) \quad (\text{Equation 6})$$

where β is the tunneling parameter. Assuming⁹⁰ $\beta = 0.2 \text{ \AA}^{-1}$, with $k_s = 2.0 \times 10^{-4} (\text{cm/s})$ and $d = 0.5 \text{ nm}$, k'_s can be predicted. The results are given in table 4.

The predicted number 7.4×10^{-5} is close to the pre-determined number 2.3×10^{-5} . Because there is a lack in data points, it is hard to conclude for sure that electrons transfer through the TiO_2 layer by tunneling. If more data points are included, a curve fitting can be done to estimate the β value. And the goodness of fitting can reveal whether or not electrons transfer by tunneling.

Still, there is another interpretation of the data. If we assume that electron transfer happens because a fraction of the electrode surface is electrically active. The fractional electroactive area ($1 - \theta$) of the electrode can be estimated by the relationship⁹¹⁻⁹⁴ between the measured k'_s for electron transfer and the maximum possible electron-transfer rate (k_s) at a fully active electrode:

$$k_s'' = k_s(1 - \theta)$$

For ITO/(ALD 0.5 nm)TiO₂ electrode, k_s'' equals 2.3×10^{-5} cm/s and k_s is assumed^{79, 95} to be 1 cm/s. The fractional electroactive area $(1 - \theta)$ is determined to be 0.0023%, which is 12% of what is determined for bare ITO electrode (0.02%) with a k_s'' of 2.0×10^{-4} cm/s. This result is close to predicted film coverage of 90% with 0.5 nm TiO₂. The addition of 0.5 nm TiO₂ results in a decrease in electroactive area with 99.9977% (=1-0.0023%) of the electrode blocked. This result agrees with the observed substantial improvement in device performance by adding 0.5 nm of ALD TiO₂. But without good structural data, we really couldn't tell which model accounts for the electron transfer better.

Table 4. Summary of experimental determined and tunneling model predicted heterogeneous electron transfer rate constant (k_s) of dimethylferrocene base on the values of the peak separations.

Electrode	ΔE_p (mV)	k_s (cm/s)	d (nm)	Predicted k_s' (cm/s)
Bare ITO	147	2.0×10^{-4}	0	_____
ITO/(ALD 0.5 nm) TiO₂	399	2.3×10^{-5}	0.5	7.4×10^{-5}

The hole blocking capability of TiO₂ is also demonstrated in the J-V characteristics of Si/TiO₂ heterojunction diode devices given in figure 22. This figure is provided by the Graham group at Georgia Institute of Technology. As shown in figure 22.a, the large energy band gap of TiO₂ should block the holes in the valence band of the p-type silicon from traveling to the Al metal contact. The evidence is given in figure 22.b, where the J-V response of the Al/TiO₂/p-type Si/Ag device (black line) shows clear rectifying behavior

while the J-V response of the Al/TiO₂/n-type Si/Ag device (red line) shows no rectification but only evidence of higher series resistance compared with both types of Ag/Si/TiO_x/Al devices (green line).

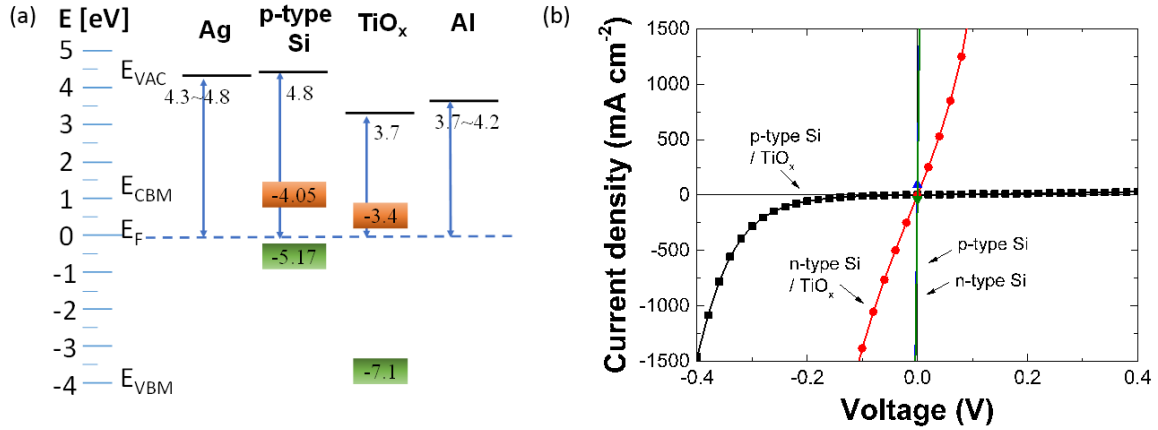


Figure 22. (a) Proposed general band energy diagram of Ag/p-type Si/TiO_x/Al test device structures. (b) Current density-voltage (J-V) characteristics of Al/p-type Si/Ag or Al/n-type Si/Ag devices with or without 3 nm TiO₂ hole-blocking layer between the Al contact and Si.

In summary, it is discovered that the charge transfer blocking capability achieved by 0.5 nm ALD TiO₂ is evident and by 3 and 10 nm ALD TiO₂ films is so effective that it is equivalent to what was reported for 12, 24, and 36 nm thick CVD TiO₂ films.⁴⁸ This result, coupled with CAFM and XPS findings, has first time demonstrated a way of preparing ultrathin pinhole free TiO₂ films for OPV application.

3.4 Device Characterization

Figure 23 shows the dark and light J-V curves of photovoltaic devices with a configuration of ITO/TiO₂/P₃HT:PC₆₁BM/PEDOT: PSS/Ag. Figure 24 shows the device configuration and its band diagram. Table 4 summarizes the device characteristics of the devices consist of different TiO₂ interlayers. Devices with 3 nm ALD TiO₂ and 24 nm CVD TiO₂ showed the smallest leakage current (Figure 23a) and the largest shunt resistance (Table 4). Devices with 3 and 10 nm ALD TiO₂ showed the smallest series resistance and largest fill factor. The local ideality factor is a measure of the slope of the J–V characteristics on a semi-logarithmic plot. The ideality factor of the device is determined from the plateau in the Ideality factor – Voltage characteristics.⁹⁶ The increase of ideality factor in the low voltage region is an indication of small shunt resistance. Ideality factor – Voltage characteristics calculated for the photovoltaic devices with ALD TiO₂ films of different thicknesses are given in figure 25. With large shunt resistance, small series resistance, large fill factor and an ideality factor closest to 2 in the low voltage region, devices with 3 nm ALD TiO₂ turned out to be the ones with the highest average efficiency at 3.0%.

The large shunt resistance of devices with TiO₂ film compared to devices made with bare ITO confirmed that the TiO₂ films were effective hole blocking interlayers.⁴⁸ The shunt resistance of device increases as the thickness of ALD TiO₂ interlayer increases from 1 nm to 3 nm, meanwhile, the shunt resistance decreases as the thickness ALD TiO₂ interlayer increases from 3 nm to 10 nm. This trend is consistent with the observed conductivity measured by CAFM for ITO/TiO₂ substrates. Of all samples with ALD TiO₂, the least conductive samples are ITO/(ALD 3 nm)TiO₂ substrates and the devices with largest shunt

resistances are the ones with 3 nm TiO₂ interlayer as well. This correlation suggests that the CAFM measured current magnitude is an indication of device shunt resistance. This is reasonable because the direction at which the electrons flow in CAFM measurement is the same as the direction electrons flow in a leakage current. Large shunt resistance goes hand in hand with small leakage current, and therefore, high device efficiency. As we could see from the intercepts between the log J-V curves and the current axis in figure 23.a, the devices with 3 nm ALD TiO₂ and 24 nm CVD TiO₂ films yield the smallest leakage current. However, while devices with 24 nm CVD TiO₂ bear large shunt resistance, they do not exhibit high efficiency. This is due to the relatively large series resistance resulted from large film thickness. ALD TiO₂ films have successfully proved its merit by exhibiting OPV devices with not only large shunt resistances but also small series resistances.

Table 5. Summary of ITO/TiO₂/P₃HT:PC₆₁BM/PEDOT: PSS/Ag photovoltaic device characteristics with different TiO₂ interlayers. 0.5, 1, 3 and 10 nm thick TiO₂ interlayers were ALD films and 24 nm thick TiO₂ interlayer was CVD film. Shunt resistance (R_p) is estimated from the inverted slope of light J-V curves at -1.0 V. Series resistance (R_s) is estimated from the inverted slope of light J-V curves at +1.0 V. The local ideality factor (n) of the device is determined in the low voltage region.

<i>TiO₂</i> <i>thickness</i>	<i>V_{oc}</i> (V)	<i>J_{sc}</i> (mA/cm²)	<i>FF</i>	<i>PCE</i> (%)	<i>R_p</i> (kΩcm²)	<i>R_s</i> (Ωcm²)	<i>n</i>
<i>0.5 nm</i>	0.612 ± 0.006	-9.24 ± 0.04	0.48 ± 0.1	2.7 ± 0.1	0.6 ± 0.2	27 ± 1	10 ± 2
<i>1 nm</i>	0.623 ± 0.004	-9.6 ± 0.3	0.47 ± 0.1	2.8 ± 0.1	1.2 ± 0.5	19 ± 1	8 ± 2
<i>3 nm</i>	0.623 ± 0.003	-9.3 ± 0.2	0.51 ± 0.2	3.0 ± 0.1	4 ± 3	18 ± 1	1.9 ± 0.7
<i>10 nm</i>	0.615 ± 0.002	-9.0 ± 0.1	0.50 ± 0.1	2.7 ± 0.1	1.0 ± 0.3	11 ± 1	3.1 ± 1.0

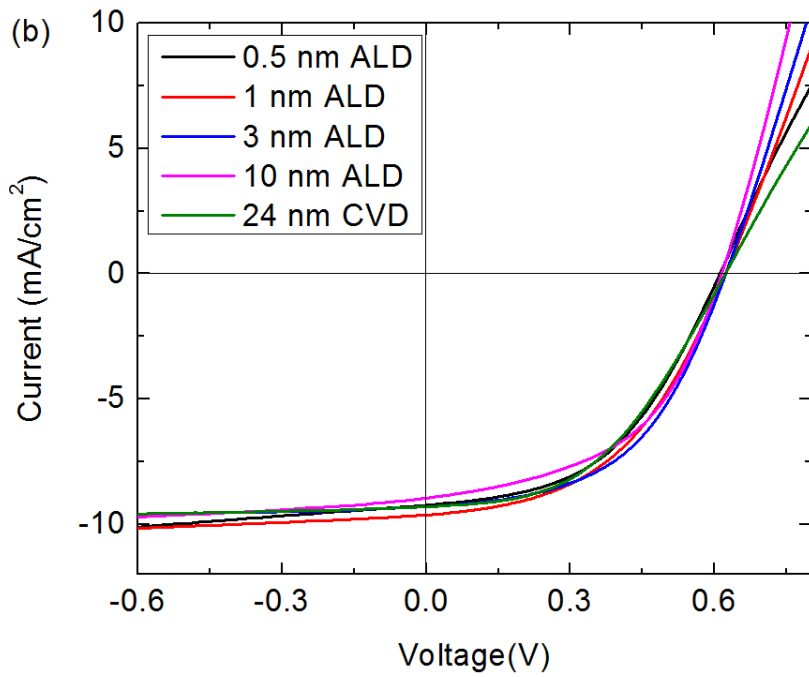
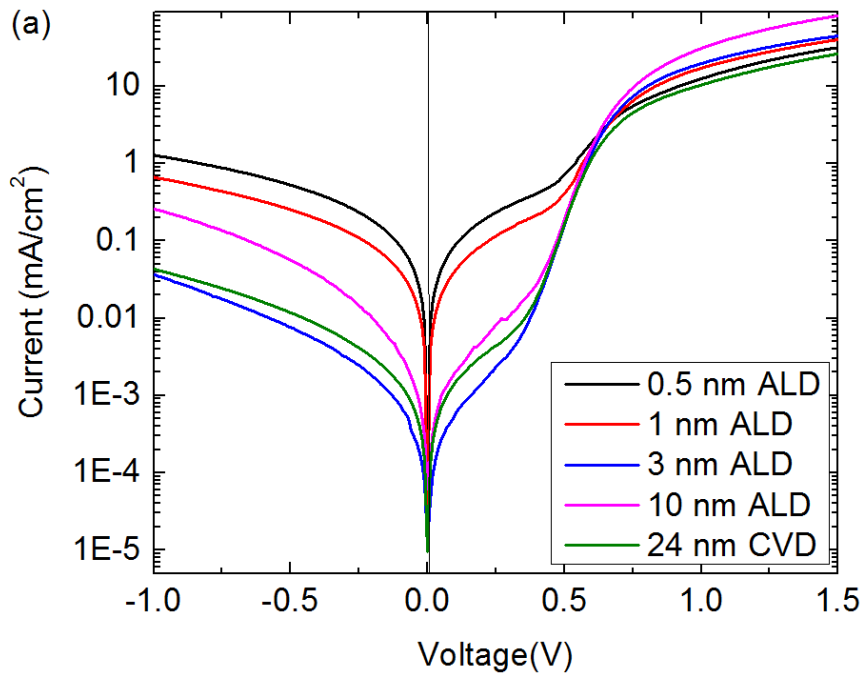


Figure 23. Current density-voltage characteristics of ITO/TiO₂/P₃HT:PC₆₁BM/PEDOT:PSS/Ag photovoltaic devices with different TiO₂ interlayers. (a) Log *J-V* curves under dark conditions. (b) Linear *J-V* curves under illumination.

The increase in shunt resistance from devices with 0.5 nm to 3 nm TiO₂ film is related to thicker and better film coverage as shown in CAFM and CV results. The decrease in shunt resistance from devices with 3 nm to 10 nm TiO₂ film could be related to the change in crystalline structure. Hyungchul Kim in the Graham group analyzed the ALD TiO₂ film on Si substrate with XRD (figure 16). It turned out that the 10 nm thick ALD TiO₂ film is anatase while the others are amorphous. And new conductive hot spots are observed in CAFM images for the ITO/(ALD 10 nm)TiO₂ samples. Researchers have shown that anatase TiO₂ is more conductive than amorphous TiO₂⁷³⁻⁷⁴ and grain boundaries in anatase TiO₂ were reported to provide electron paths resulting in high leakage current.⁹⁷⁻⁹⁸ This relates the observed change in crystalline structure to the decrease in shunt resistance. The power conversion efficiency of dye-sensitized solar cells from Meyer's group peaked with 2.4 nm ALD TiO₂ and decreases as ALD TiO₂ layer gets thicker⁶⁶. Our discovery agrees with their result that there is an optimum thickness before ALD TiO₂ layer gets thicker and gets better at back electron transfer.

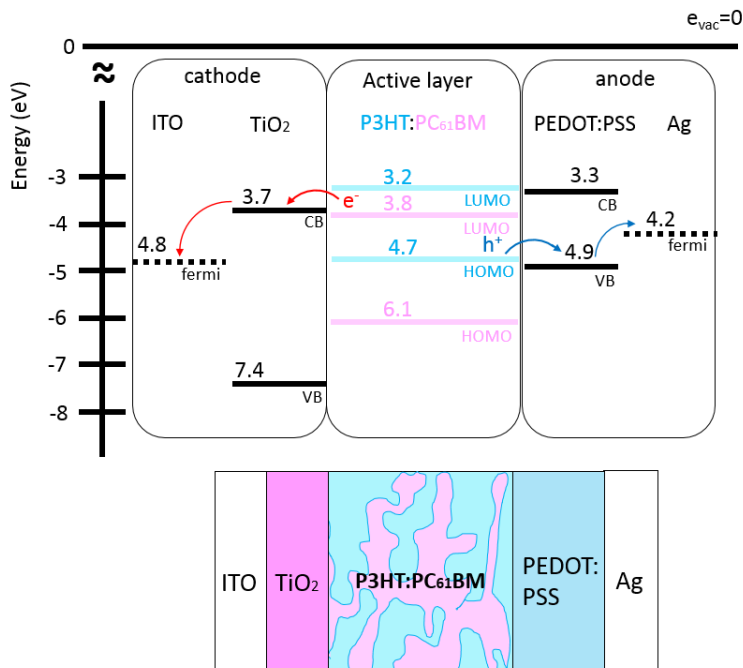


Figure 24. Device configuration (bottom) of ITO/TiO₂/P₃HT: PC₆₁BM/PEDOT: PSS/Ag photovoltaic devices and its proposed band diagram (top) from literature values.

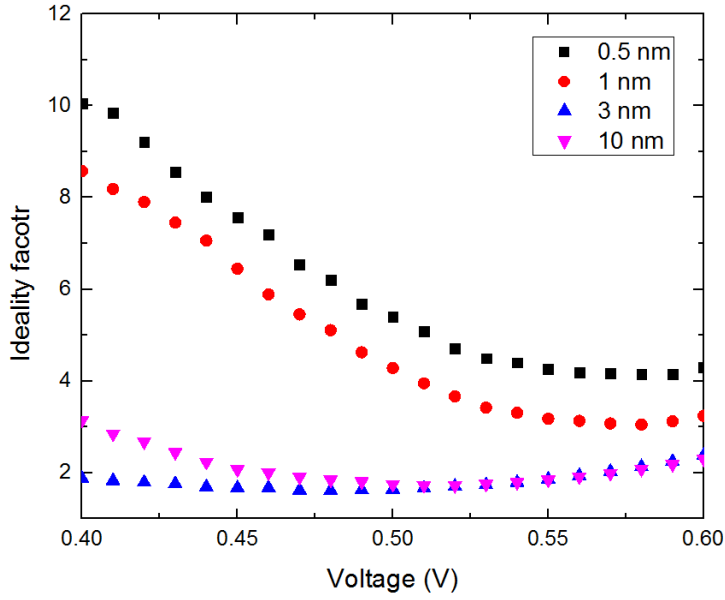


Figure 25. Ideality factor – Voltage characteristics calculated for the photovoltaic devices with ALD TiO₂ films of different thicknesses.

Chapter 4: Conclusions and Future Directions

4.1 Conclusions

For the first time, TiO₂ films deposited by atomic layer deposition have been used as electron collecting interlayers for organic photovoltaics. The ALD TiO₂ film properties were characterized and compared with those of CVD TiO₂ film. The morphology data from CAFM shows that both methods were able to deliver films of conformal coverage. The average current magnitudes obtained with ITO/(ALD)TiO₂ substrates from CAFM indicate that ITO/(ALD 3 nm)TiO₂ substrate is the least conductive. XPS results show that both CVD and ALD TiO₂ contains Ti⁴⁺ species and oxygen from hydroxyl groups. Cyclic voltammograms of probe molecules with ITO substrates covered by 3 nm and 10 nm thick TiO₂ films indicate a pinhole free coverage and effective hole blocking capability of the TiO₂ films. Devices with ultrathin 3 nm ALD TiO₂ films achieved higher efficiencies than those with 24 nm CVD TiO₂ films. Results from organic photovoltaic devices correlate well with film properties characterized by the above methods. It is clear that ALD was able to deposit films with even better conformality than CVD. There are several aspects that contribute to this result. The atomic layer deposition is a two-step self-limiting process. It eliminates any gas phase homogeneous reactions. And it controls the surface reaction on a layer to layer basis. Incoming reactant molecules are introduced only after the by-products from the surface reaction have been purged out of the chamber. While in the CVD process, continuous reaction on the surface would more likely to result in trapped by-products and porosity formation.⁶³ The improvement in film quality is huge such that the ultrathin 3 nm ALD TiO₂ films exhibit more desirable properties than 24 nm CVD TiO₂ films. Besides delivering films with competitive properties with this surprisingly small film thickness, it

is also important that ALD enables us to obtain extremely conformal and pin-hole free TiO₂ films prepared at low temperature (250°C) compared to other methods (450°C).^{41, 52} And it is amazing that even 0.5 nm of TiO₂ film is able to improve the device substantially and provide devices with efficiencies comparable to those perform the best. To deposit 0.5 nm of TiO₂, 10 ALD deposition cycles are needed. With one fifth of monolayer coverage per cycle,⁶³ 0.5 nm of TiO₂ would achieve 90% monolayer coverage. With the fractional electroactive area of bare ITO electrode determined to be 0.02%,⁷⁹ 0.5 nm of TiO₂ film is able to achieve a decreased electroactive area with 99.9977% of the electrode blocked. This explains how the excellent conformality and pin-hole free coverage provided by ALD TiO₂ make a difference and why these 0.5 nm of TiO₂ films are so good electronically for OPV devices.

The hypothesis that ALD would be able to create TiO₂ films that constitute organic photovoltaic devices with not only large shunt resistance but also small series resistance is tested. And we conclude that ALD is an effective way of manufacturing ultrathin conformal TiO₂ films for improved organic photovoltaic devices.

4.2 Future Directions

A better designed and manufactured interlayer could continue to improve OPV performance and stability. The future improvement of ALD TiO₂ films may require the introduction of dopants or other post deposition treatment, which will have significant impact on the chemical and electronic properties of the films. To make the deposition process of TiO₂ films by ALD compatible with flexible substrates, lower deposition temperature should be explored.

References

1. Riordan, C.; Hulstron, R. In *What is an air mass 1.5 spectrum? [solar cell performance calculations]*, Photovoltaic Specialists Conference, 1990., Conference Record of the Twenty First IEEE, 21-25 May 1990; 1990; pp 1085-1088 vol.2.
2. Shockley, W.; Queisser, H. J., *J. Appl. Phys.* **1961**, 32 (3), 510.
3. Vos, A. D., *J. Phys. D: Appl. Phys.* **1980**, 13 (5), 839.
4. Blom, P. W. M.; Mihailetschi, V. D.; Koster, L. J. A.; Markov, D. E., *Adv. Mater. (Weinheim, Ger.)* **2007**, 19 (12), 1551-1566.
5. Ameri, T.; Dennler, G.; Lungenschmied, C.; Brabec, C. J., *Energy & Environmental Science* **2009**, 2 (4), 347.
6. Walzer, K.; Maennig, B.; Pfeiffer, M.; Leo, K., *Chem. Rev. (Washington, DC, U. S.)* **2007**, 107 (4), 1233-1271.
7. Günes, S.; Neugebauer, H.; Sariciftci, N. S., *Chem. Rev. (Washington, DC, U. S.)* **2007**, 107 (4), 1324-1338.
8. Forrest, S. R., *MRS Bulletin* **2005**, 30 (01), 28-32.
9. Brédas, J.-L.; Norton, J. E.; Cornil, J.; Coropceanu, V., *Acc. Chem. Res.* **2009**, 42 (11), 1691-1699.
10. Cheng, Y.-J.; Yang, S.-H.; Hsu, C.-S., *Chem. Rev. (Washington, DC, U. S.)* **2009**, 109 (11), 5868-5923.
11. Servaites, J. D.; Ratner, M. A.; Marks, T. J., *Energy & Environmental Science* **2011**, 4 (11), 4410.
12. Mazziio, K. A.; Luscombe, C. K., *Chem. Soc. Rev.* **2015**, 44 (1), 78-90.
13. Hoppe, H.; Sariciftci, N. S., *J. Mater. Res.* **2011**, 19 (07), 1924-1945.

14. Li, G.; Chu, C. W.; Shrotriya, V.; Huang, J.; Yang, Y., *Appl. Phys. Lett.* **2006**, *88* (25), 253503.
15. Yu, B. Y.; Tsai, A.; Tsai, S. P.; Wong, K. T.; Yang, Y.; Chu, C. W.; Shyue, J. J., *Nanotechnology* **2008**, *19* (25), 255202.
16. Hau, S. K.; Yip, H.-L.; Baek, N. S.; Zou, J.; O'Malley, K.; Jen, A. K. Y., *Appl. Phys. Lett.* **2008**, *92* (25), 253301.
17. Jørgensen, M.; Norrman, K.; Krebs, F. C., *Sol. Energy Mater. Sol. Cells* **2008**, *92* (7), 686-714.
18. Park, J. H.; Lee, T. W.; Chin, B. D.; Wang, D. H.; Park, O. O., *Macromol. Rapid Commun.* **2010**, *31* (24), 2095-108.
19. Norrman, K.; Larsen, N. B.; Krebs, F. C., *Sol. Energy Mater. Sol. Cells* **2006**, *90* (17), 2793-2814.
20. Gao, Y., *Materials Science and Engineering: R: Reports* **2010**, *68* (3), 39-87.
21. Meyer, J.; Hamwi, S.; Kroger, M.; Kowalsky, W.; Riedl, T.; Kahn, A., *Adv Mater* **2012**, *24* (40), 5408-27.
22. Li, Z.; Meng, W.; Tong, J.; Zhao, C.; Qin, F.; Jiang, F.; Xiong, S.; Zeng, S.; Xu, L.; Hu, B.; Zhou, Y., *Sol. Energy Mater. Sol. Cells* **2015**, *137*, 311-318.
23. Shrotriya, V.; Li, G.; Yao, Y.; Chu, C.-W.; Yang, Y., *Appl. Phys. Lett.* **2006**, *88* (7), 073508.
24. Ratcliff, E. L.; Meyer, J.; Steirer, K. X.; Armstrong, N. R.; Olson, D.; Kahn, A., *Organic Electronics* **2012**, *13* (5), 744-749.
25. Tan, Z. a.; Li, L.; Cui, C.; Ding, Y.; Xu, Q.; Li, S.; Qian, D.; Li, Y., *J. Phys. Chem. C* **2012**, *116* (35), 18626-18632.

26. Tao, C.; Ruan, S.; Zhang, X.; Xie, G.; Shen, L.; Kong, X.; Dong, W.; Liu, C.; Chen, W., *Appl. Phys. Lett.* **2008**, *93* (19), 193307.
27. Brabec, C. J.; Shaheen, S. E.; Winder, C.; Sariciftci, N. S.; Denk, P., *Appl. Phys. Lett.* **2002**, *80* (7), 1288.
28. Liao, H.-H.; Chen, L.-M.; Xu, Z.; Li, G.; Yang, Y., *Appl. Phys. Lett.* **2008**, *92* (17), 173303.
29. Scharber, M. C.; Sariciftci, N. S., *Prog. Polym. Sci.* **2013**, *38* (12), 1929-1940.
30. de Jong, M. P.; van Ijzendoorn, L. J.; de Voigt, M. J. A., *Appl. Phys. Lett.* **2000**, *77* (14), 2255.
31. Waldauf, C.; Morana, M.; Denk, P.; Schilinsky, P.; Coakley, K.; Choulis, S. A.; Brabec, C. J., *Appl. Phys. Lett.* **2006**, *89* (23), 233517.
32. Takanezawa, K.; Hirota, K.; Wei, Q.-S.; Tajima, K.; Hashimoto, K., *J. Phys. Chem. C* **2007**, *111* (19), 7218-7223.
33. Steim, R.; Kogler, F. R.; Brabec, C. J., *J. Mater. Chem.* **2010**, *20* (13), 2499.
34. Ratcliff, E. L.; Zacher, B.; Armstrong, N. R., *J. Phys. Chem. L* **2011**, *2* (11), 1337-1350.
35. Ma, H.; Yip, H.-L.; Huang, F.; Jen, A. K. Y., *Adv. Funct. Mater.* **2010**, *20* (9), 1371-1388.
36. Lee, K.; Kim, J. Y.; Park, S. H.; Kim, S. H.; Cho, S.; Heeger, A. J., *Adv. Mater. (Weinheim, Ger.)* **2007**, *19* (18), 2445-2449.
37. Li, J.; Kim, S.; Edington, S.; Nedy, J.; Cho, S.; Lee, K.; Heeger, A. J.; Gupta, M. C.; Yates Jr, J. T., *Sol. Energy Mater. Sol. Cells* **2011**, *95* (4), 1123-1130.

38. Kuwabara, T.; Nakayama, T.; Uozumi, K.; Yamaguchi, T.; Takahashi, K., *Sol. Energy Mater. Sol. Cells* **2008**, *92* (11), 1476-1482.
39. Schumann, S.; Da Campo, R.; Illy, B.; Cruickshank, A. C.; McLachlan, M. A.; Ryan, M. P.; Riley, D. J.; McComb, D. W.; Jones, T. S., *J. Mater. Chem.* **2011**, *21* (7), 2381-2386.
40. Yip, H.-L.; Jen, A. K. Y., *Energy & Environmental Science* **2012**, *5* (3), 5994.
41. Yuan, S.; Zhang, Y.; Liu, W.; Zhang, W., *Electrochim. Acta* **2014**, *116*, 442-446.
42. Akpan, U. G.; Hameed, B. H., *Applied Catalysis A: General* **2010**, *375* (1), 1-11.
43. Abdullah, M. H.; Rusop, M., *J. Alloys Compd.* **2014**, *600*, 60-66.
44. Macwan, D. P.; Dave, P. N.; Chaturvedi, S., *J. Mater. Sci.* **2011**, *46* (11), 3669-3686.
45. Zhang, W.-z.; Zhang, T.; Yin, W.; Cao, G.-y., *Chin. J. Chem. Phys.* **2007**, *20* (1), 95-98.
46. Chen, X.; Mao, S. S., *Chem. Rev. (Washington, DC, U. S.)* **2007**, *107* (7), 2891-2959.
47. Jiang, Z.; Yang, D.; Wang, N.; Zhang, F.; Zhao, B.; Tan, S.; Zhang, J., *Science China Chemistry* **2013**, *56* (11), 1573-1577.
48. Ou, K.-L.; Tadytin, D.; Xerxes Steirer, K.; Placencia, D.; Nguyen, M.; Lee, P.; Armstrong, N. R., *Journal of Materials Chemistry A* **2013**, *1* (23), 6794.
49. Salim, T.; Yin, Z.; Sun, S.; Huang, X.; Zhang, H.; Lam, Y. M., *ACS Appl. Mater. Interfaces* **2011**, *3* (4), 1063-7.
50. Niederberger, M. P., N., *Metal Oxide Nanoparticles in Organic Solvents: Synthesis, Formation, Assembly and Application*. Springer: 2009.

51. Lazim, H. G.; Ajeel, K. I.; Badran, H. A., *Spectrochimica acta. Part A, Molecular and biomolecular spectroscopy* **2015**, *145*, 598-603.
52. Lewkowicz, A.; Synak, A.; Grobelna, B.; Bojarski, P.; Bogdanowicz, R.; Karczewski, J.; Szczodrowski, K.; Behrendt, M., *Optical Materials* **2014**, *36* (10), 1739-1744.
53. Kim, J. Y.; Kim, S. H.; Lee, H. H.; Lee, K.; Ma, W.; Gong, X.; Heeger, A. J., *Adv. Mater. (Weinheim, Ger.)* **2006**, *18* (5), 572-576.
54. Niu, W.; Li, X.; Karuturi, S. K.; Fam, D. W.; Fan, H.; Shrestha, S.; Wong, L. H.; Tok, A. I., *Nanotechnology* **2015**, *26* (6), 064001.
55. Jin, S. H.; Jun, G. H.; Hong, S. H.; Jeon, S., *Carbon* **2012**, *50* (12), 4483-4488.
56. Wu, Y.; Yang, X.; Chen, H.; Zhang, K.; Qin, C.; Liu, J.; Peng, W.; Islam, A.; Bi, E.; Ye, F.; Yin, M.; Zhang, P.; Han, L., *Applied Physics Express* **2014**, *7* (5), 052301.
57. Vasilopoulou, M.; Konofaos, N.; Davazoglou, D.; Argitis, P.; Stathopoulos, N. A.; Savaidis, S. P.; Iliadis, A. A., *Solid-State Electron.* **2014**, *101* (0), 50-56.
58. Jones, A. C.; Aspinall, H. C.; Chalker, P. R., **2008**, 357-412.
59. Aarik, J.; Aidla, A.; Uustare, T.; Ritala, M.; Leskelä M., *Appl. Surf. Sci.* **2000**, *161* (3-4), 385-395.
60. Yan, X.-T.; Yongdong, X., *Chemical vapour deposition: an integrated engineering design for advanced materials*. Springer: New York; London, 2010.
61. Choy, K. L., *Progress in Materials Science* **2003**, *48* (2), 57-170.
62. Jones, A. C.; Hitchman, M. L.; Royal Society of, C., *Chemical vapour deposition: precursors, processes and applications*. Royal Society of Chemistry: Cambridge, UK, 2009.

63. Kaariainen, T.; ebrary, I., *Atomic layer deposition: principles, characteristics, and nanotechnology applications*. John Wiley & Sons: Hoboken, NJ 2013.
64. Potts, S. E.; Keuning, W.; Langereis, E.; Dingemans, G.; van de Sanden, M. C. M.; Kessels, W. M. M., *J. Electrochem. Soc.* **2010**, *157* (7), P66-P74.
65. Xie, Q.; Musschoot, J.; Deduytsche, D.; Van Meirhaeghe, R. L.; Detavernier, C.; Van den Berghe, S.; Jiang, Y.-L.; Ru, G.-P.; Li, B.-Z.; Qu, X.-P., *J. Electrochem. Soc.* **2008**, *155* (9), H688-H692.
66. Alibabaei, L.; Farnum, B. H.; Kalanyan, B.; Brennaman, M. K.; Losego, M. D.; Parsons, G. N.; Meyer, T. J., *Nano Lett.* **2014**, *14* (6), 3255-3261.
67. Alibabaei, L.; Sherman, B. D.; Norris, M. R.; Brennaman, M. K.; Meyer, T. J., *Proceedings of the National Academy of Sciences* **2015**, *112* (19), 5899-5902.
68. Alibabaei, L.; Brennaman, M. K.; Norris, M. R.; Kalanyan, B.; Song, W.; Losego, M. D.; Concepcion, J. J.; Binstead, R. A.; Parsons, G. N.; Meyer, T. J., *Proceedings of the National Academy of Sciences* **2013**, *110* (50), 20008-20013.
69. Aarik, L.; Arroval, T.; Rammula, R.; M ändar, H.; Sammelseg, V.; Aarik, J., *Thin Solid Films* **2013**, *542*, 100-107.
70. Aarik, J.; Karlis, J.; M ändar, H.; Uustare, T.; Sammelseg, V., *Appl. Surf. Sci.* **2001**, *181* (3-4), 339-348.
71. Mitchell, D. R. G.; Attard, D. J.; Triani, G., *Thin Solid Films* **2003**, *441* (1-2), 85-95.
72. Langereis, E.; Heil, S. B. S.; Knoop, H. C. M.; Keuning, W.; Sanden, M. C. M. v. d.; Kessels, W. M. M., *J. Phys. D: Appl. Phys.* **2009**, *42* (7), 073001.

73. Shih, W. S.; Young, S. J.; Ji, L. W.; Water, W.; Shiu, H. W., *J. Electrochem. Soc.* **2011**, *158* (6), H609.
74. *Journal of the Korean Vacuum Society* **2010**, *19* (2), 105.
75. Sayers, C. N.; Armstrong, N. R., *Surf. Sci.* **1978**, *77* (2), 301-320.
76. Wang, R.; Sakai, N.; Fujishima, A.; Watanabe, T.; Hashimoto, K., *J. Phys. Chem. B* **1999**, *103* (12), 2188-2194.
77. Tahir, M.; Amin, N. S., *Applied Catalysis B: Environmental* **2015**, *162*, 98-109.
78. Minato, T.; Sainoo, Y.; Kim, Y.; Kato, H. S.; Aika, K.-i.; Kawai, M.; Zhao, J.; Petek, H.; Huang, T.; He, W.; Wang, B.; Wang, Z.; Zhao, Y.; Yang, J.; Hou, J. G., *The Journal of Chemical Physics* **2009**, *130* (12), 124502.
79. Brumbach, M.; Veneman, P. A.; Marrikar, F. S.; Schulmeyer, T.; Simmonds, A.; Xia, W.; Lee, P.; Armstrong, N. R., *Langmuir* **2007**, *23* (22), 11089-11099.
80. Zhang, Z.; Bondarchuk, O.; Kay, B. D.; White, J. M.; Dohnálek, Z., *J. Phys. Chem. B* **2006**, *110* (43), 21840-21845.
81. Abbas, H.; Nasser, S. A., *J. Power Sources* **1996**, *58* (1), 15-21.
82. Amore Bonapasta, A.; Filippone, F.; Mattioli, G.; Alippi, P., *Catal. Today* **2009**, *144* (1-2), 177-182.
83. Eom, S. H.; Baek, M.-J.; Park, H.; Yan, L.; Liu, S.; You, W.; Lee, S.-H., *ACS Appl. Mater. Interfaces* **2014**, *6* (2), 803-810.
84. Lattante, S., *Electronics* **2014**, *3* (1), 132-164.
85. Satpati, A. K.; Arroyo-Currás, N.; Ji, L.; Yu, E. T.; Bard, A. J., *Chem. Mater.* **2013**, *25* (21), 4165-4172.
86. Nicholson, R. S., *Anal. Chem.* **1965**, *37* (11), 1351-1355.

87. Perone, S. P., *Anal. Chem.* **1966**, 38 (9), 1158-1163.
88. Zhou, H.; Gu, N.; Dong, S., *J. Solid State Electrochem.* **1999**, 3 (2), 82-86.
89. Finklea, H. O.; Hanshew, D. D., *J. Am. Chem. Soc.* **1992**, 114 (9), 3173-3181.
90. Moffat, T. P.; Yang, H.; Fan, F. R. F.; Bard, A. J., *J. Electrochem. Soc.* **1992**, 139 (11), 3158-3167.
91. Amatore, C.; Sav éant, J. M.; Tessier, D., *Journal of Electroanalytical Chemistry and Interfacial Electrochemistry* **1983**, 147 (1-2), 39-51.
92. Amatore, C.; Sav éant, J. M.; Tessier, D., *Journal of Electroanalytical Chemistry and Interfacial Electrochemistry* **1983**, 146 (1), 37-45.
93. Duo, I.; Fujishima, A.; Comninellis, C., *Electrochem. Commun.* **2003**, 5 (8), 695-700.
94. Holt, K. B.; Bard, A. J.; Show, Y.; Swain, G. M., *J. Phys. Chem. B* **2004**, 108 (39), 15117-15127.
95. Marrikar, F. S.; Brumbach, M.; Evans, D. H.; Lebr ón-Paler, A.; Pemberton, J. E.; Wysocki, R. J.; Armstrong, N. R., *Langmuir* **2007**, 23 (3), 1530-1542.
96. Wetzelaer, G.-J. A. H.; Scheepers, M.; Sempere, A. M.; Momblona, C.; Ávila, J.; Bolink, H. J., *Adv. Mater. (Weinheim, Ger.)* **2015**, 27 (11), 1837-1841.
97. Dang, V.-S.; Parala, H.; Kim, J. H.; Xu, K.; Srinivasan, N. B.; Edengeiser, E.; Havenith, M.; Wieck, A. D.; de los Arcos, T.; Fischer, R. A.; Devi, A., *physica status solidi (a)* **2014**, 211 (2), 416-424.
98. Shin, H.; De Guire, M. R.; Heuer, A. H., *J. Appl. Phys.* **1998**, 83 (6), 3311-3317.